arXiv:astro-ph/0312002v1 28 Nov 2003

Investigating the Origins of Dark Matter Halo Density Profiles

Liliya L.R. Williams

Astronomy Department, University of Minnesota, Minneapolis, MN 55455

llrw@astro.umn.edu

Arif Babul[1]

Department of Physics and Astronomy, University of Victoria, BC, Canada

babul@uvic.ca

Julianne J. Dalcanton[2]

Astronomy Department, University of Washington, Box 351580, Seattle, WA 98195

jd@astro.washington.edu

ABSTRACT

Although high-resolution N-body simulations make robust empirical predictions for the density distribution within cold dark matter halos, these studies have yielded little physical insight into the origins of the distribution. We therefore attempt to investigate the problem using analytic and semi-analytic approaches. Simple analytic considerations suggest that the inner slope of the central cusps in dark matter halos cannot be steeper than $\alpha = 2$ (where $\rho \propto r^{-\alpha}$), with $\alpha = 1.5$–1.7 being a more realistic upper limit. Moreover, our analysis suggests that any number of effects, whether real (eg. angular momentum imparted by tidal torques and secondary perturbations) or artificial (eg. two-body interactions, the accuracy of the numerical integrator, round-off errors), will result in shallower slopes. We also find that the halos should exhibit a well-defined relationship between r_{peri}/r_{apo} and j_θ/j_r. We derive this relationship analytically and speculate that it may be "universal". Using a semi-analytic scheme based on Ryden & Gunn (1987), we further explore the relationship between the specific angular momentum distribution in a halo and its density profile. For present purposes,

[1]CITA Senior Fellow

[2]Alfred P. Sloan Foundation Fellow

we restrict ourselves to halos that form primarily via nearly-smooth accretion of matter, and only consider the specific angular momentum generated by secondary perturbations associated with the cold dark matter spectrum of density fluctuations. Compared to those formed in N-body simulations, our "semi-analytic" halos are more extended, have flatter rotation curves and have higher specific angular momentum, even though we have not yet taken into account the effects of tidal torques. Whether the density profile of numerical halos is indeed the result of loss in angular momentum outside the central region, and whether this loss is a feature of hierarchical merging and major mergers in particular, is under investigation.

Subject headings: cosmology: dark matter — galaxies: formation, evolution

1. Introduction

Over the past two decades, observational and theoretical progress have given rise to an increasingly detailed picture of how structure in the Universe forms and evolves. In the prevailing paradigm for the formation of structure in the Universe, galaxies and clusters of galaxies are contained within extended cold dark matter (CDM) halos, formed hierarchically through gravitationally induced mergers of smaller-scale structure. The evolution of individual dark matter halos and the formation of galactic structure inside the halos is strongly dependent on a daunting array of physical processes that span a wide range of scales. It is not surprising, therefore, that even the very first steps in the assembly of galaxies – the details of how dark halos form and virialize, the shape and profile of their equilibrium structure, and the extent to which that structure is shaped by the surrounding large-scale structure and the halo's merger history – are not well understood.

At the simplest level, dark matter halos form when, in the early Universe, the matter within (and surrounding) an overdense region suffers gravitational retardation, decouples from the Hubble flow, collapses, and in due course, virializes. The basic theoretical framework underlying the above sequence was outlined by Gunn & Gott (1972), Gott (1975) and Gunn (1977), and subsequently elaborated upon by Fillmore & Goldreich (1984) and Hoffman & Shaham (1985). In order to make the problem analytically tractable, several simplifications had to be invoked, including spherical symmetry, purely radial particle orbits, and power-law initial density profiles. These studies predicted power-law halo density profiles, $\rho(r) \propto r^{-\alpha}$, with index α ranging from 2 to 2.25. These initial results were encouraging in that the density profile, at the very least, could explain the nearly flat rotation curves of massive spiral galaxies.

In a bid to relax the restrictive assumptions underlying the analytic investigations and to incorporate the full range of non-linear gravitational effects, Quinn, Salmon & Zurek (1986) pioneered the use of N-body simulations to study halo formation. Subsequent higher resolution simulations by Frenk *et al.* (1988), Dubinski & Carlberg (1991), Navarro, Frenk & White (1996, 1997, hereafter NFW), Moore *et al.* (1998) Jing & Suto (2000), Klypin *et al.* (2001), Bullock *et al.* (2001), and Power *et al.* (2003) found that although the spherically-averaged density profiles of the N-body dark matter halos are similar regardless of the mass of the halo or the cosmological model, they are significantly different from the single power laws predicted by the theoretical studies. The N-body profiles are characterized by an r^{-3} decline at large radii and a cuspy profile of the form $\rho(r) \propto r^{-\alpha}$ where $\alpha < 2$ near the center. The actual value of the inner density slope α is a matter of some controversy, with NFW and Power *et al.* (2002) suggesting $\alpha = 1$, but with Moore *et al.* (1998), Ghigna *et al.* (2000) and Fukushige & Makino (2001) arguing for $\alpha = 1.5$. Klypin *et al.* (2001) argue that NFW and Moore *et al.* profiles are compatible with each other, within their range of applicability: the profile can only be trusted beyond radii which are 2-4 times larger than the formal resolution of the simulation.

In spite of the controversy about the exact slope of the cusp at the center of the simulated halos the "universal" N-body density profiles have been widely adopted for theoretical work. The analytic form for the profile is simple and easy to work with, and does have some observational support on the scale of clusters (*e.g.* Carlberg *et al.* 1997). However, there are two important unresolved issues that require attention.

While numerical simulations universally produce the aforementioned cuspy density profiles, nature apparently does not. The predicted profiles appear to disagree with observed dark matter profiles, in both overall density and in shape, particularly at smaller mass scales. Some of the strongest evidence of the failure of the universal N-body profiles comes from observations of the dynamics of spiral galaxies. There is mounting evidence from rotation curve studies that unlike galaxies in simulations, late-type galaxies may be embedded within halos that have shallow dark matter cores (Salucci 2001; Salucci & Burkert 2000; Hernandez *et al.* 2001). Within low surface brightness (LSB) galaxies, the difference between the observed rotation curves and those predicted by N-body halo profiles becomes even more severe (*e.g.* Swaters *et al.* 2000; Dalcanton & Bernstein 2000; van den Bosch & Swaters 2001; de Blok *et al.* 2001; de Blok & Bosma 2002; Marschesini *et al.* 2002; Weldrake *et al.* 2002; Swaters *et al.* 2002); the cores of these galaxies are much less dense than the simulations indicate. These LSB galaxies are thought to be ideal for the comparison with theory, as their dynamics are dominated by dark matter with little contribution from baryons (Bothun *et al.* 1997), and thus the discrepancy with simulations is particularly troublesome.

Quite apart from the apparent discrepancies between numerical results and observations, there is yet another problem, on which very little light has been shed in spite of the tremendous progress achieved by numerical work: What is the physics underlying the universal density profiles predicted by simulations? There have been several attempts in the literature to explain the shapes of virialized halos. Intuitively, one could argue that the major difference between earlier analytical work and numerical simulations is that halo formation in N-body simulations proceeds through repeated mergers. In fact, Syer & White (1998) argue that universal N-body profile is a natural outcome of hierarchical merging. Specifically, they claim that the halo structure in the inner regions is determined by a nested sequence of undigested cores of merging substructure accumulating in the centers of the halos. However, Huss *et al.* (1999) find that simulations of isolated halos collapsing more or less spherically also result in universal profiles, thus suggesting that hierarchical merging is not crucial to the outcome. Instead, they suggest that the profile is a consequence of a near universal angular momentum distribution of the halos. Unfortunately, it is unclear what circumstances lead the halos to this universal angular momentum distribution. Thus the issue remains unresolved.

Our current state of knowledge about halos from theoretical work can be summed up as follows: universal halos are a very robust prediction of numerical N-body simulations, but we do not understand how their properties arise. This current lack of understanding of numerical halos, and hence the lack of understanding of observed galactic halos, provides the main impetus for our present and subsequent work.

In this paper we describe our dynamical method for generating virialized galaxy-scale halos, and address some basic questions regarding halo formation. Since the very large amount of work carried out by many researchers to date using N-body simulations has met with limited success in elucidating the physics of halo formation, it makes sense to consider a different approach: we use an analytical technique, pioneered by Ryden & Gunn (1987, RG87), which we describe in detail in Section 3 and Appendix A.

The most important feature of the original RG87 method is that the dynamical evolution is carried out while conserving angular and radial momenta of individual halo shells. The initial shape of the proto-halos is derived from the fluctuation spectrum at high redshifts, and halos are endowed with secondary perturbations, which impart random motions to halo particles. The statistical properties of the secondary perturbations are derived from the same fluctuation power spectrum, and therefore their effects on particles' random velocities are treated self-consistently.

In this paper we extend the RG87 method in order to more faithfully reproduce the real halos, and to allow experimentation, using a range of possible cosmological conditions.

Compared to the original RG87 formalism, our improved formalism allows the particles at a given radial location in the halo to acquire a range of velocities, not just a single rms value. The velocity distribution can be specified independently, allowing us to either constrain the distribution to be consistent with the underlying statistics of a specific dark matter model or to experiment with different distributions in order to understand the impact of non-radial and radial motions on the final structure and dynamical properties of halos.

The current version of our method treats collapse and virialization of halos that are spherically symmetric, that have suffered no major mergers or tidal torquing, and that have experienced only quiescent accretion of somewhat lumpy material, i.e. minor mergers. In this work we assume that all parts of the main halo experience statistically the same secondary perturbations, in other words, the secondary perturbation fluctuation field in unconstrained. Because our halos cannot undergo major mergers, they do not form in a fully hierarchical setting. However, the quiescent accretion scenario is worth investigating: judging by the commonness of extended thin spiral disks in the Universe, it is not far fetched to suppose that such formation histories are realistic, at least for some galaxies.

Of course, halo formation in a hierarchical scenario is a highly non-linear process. An analytical method, no matter how sophisticated, will never be able to capture the full extent of complexity of a non-linear process. And therein lies the power of the analytical approach: numerical simulations yield little physical insight beyond empirical findings precisely because they are so rich in dynamical processes, which are hard to disentangle and interpret in terms of underlying physics. We aim to complement the detailed picture of halo formation as revealed by simulations with the understanding of its broad-brush features. Put differently, we are seeking an impressionist's view of halo formation, not that of a Dutch master.

The paper is organized as follows. In Section 2 we give a broad overview of the formation of dark matter halos, and quote some major analytical results from previous work. Section 3 briefly describes the original Ryden & Gunn (1987) method, which we use a starting point for our work; a fuller description can be found in the Appendix. In Section 4 we generate virialized halos for a range of galaxy-sized halo masses. We obtain rotation curves and specific angular momentum distribution of our halos, and discuss how these relate to their N-body and observed counterparts. We also explore the role that the initial conditions play in determining the final density profile and halo dynamics. To that end, we consider fluctuation power spectra that are tilted compared to the Harrison-Zel'dovich spectrum, or are truncated at short wavelengths. In Section 5 we use the results of these experiments, combined with analytical reasoning to provide answers to some general questions about halos: why central cusps have slopes around 1-1.6, why the slope of log-log density profiles steepens monotonically from the center outward, and why virialized halos formed as a result

of quiescent accretion retain information about the shape of the primordial power spectrum.

2. Analytical treatments of dark matter halos

To put our analytical method in context we first present a broad picture of halo formation, emphasizing some of the relevant analytical work carried out to date.

In the last three to four decades a considerable amount of analytical work has been carried out to understand the formation of bound structures through gravitational instability. A number of approaches have been tried, but because of natural limitations it is difficult for any one analytical formalism to address all aspects of galaxy formation. Most papers in the literature concentrate on a specific set of initial conditions, or treat only a limited range in radii of halos. Consequently, comparison between different results is not always straightforward. Here we attempt to put together a coherent picture of the past results.

Consider an isolated halo, which has had no major mergers in its history, and divide it roughly into four regions starting from the outside: In Region (1), furthest from the center of the initial density peak, dark matter particles are beginning to feel the gravitational tug of the central peak and are just starting to fall behind the Hubble flow. Further in, in Region (2), the particles are starting to decouple from the Hubble flow and are about to begin collapse. In Region (3) the central density peak dominates the motion of particles; this is the region of infall and shell crossing. Finally, in Region (4), the central part of the density peak, virialization is taking place, or has already been reached. Note that the evolution time sequence of the halo maps roughly on to the distance away from the halo center, but the demarcation of various regions, both in time and radial distance, is only approximate. As time progresses the boundaries of all the regions in an isolated halo move out from the center, as viewed in initial comoving coordinates, i.e. the halo engulfs an ever increasing fraction of comoving volume. In an Einstein-de Sitter Universe this process can proceed indefinitely, while in a less dense universe the accretion of material is limited.

Region (1) consists of the still expanding material. Assuming spherical symmetry, Newton's first theorem says that the evolution in this region is completely determined by the matter interior to the shell. The evolution obeys a matter-dominated Friedmann equation, with the density Ω_{matter} equal to the average density inside the shell. While the shells are still expanding the well known parametric solution applies (Gunn & Gott 1972, Peebles 1980), given in equations A2 and A3 of the Appendix. The applicability of the solution ends when a given shell reaches its turn-around radius at the time when the average interior density contrast is $\sim 4-5$. The corresponding extrapolated linear density contrast is ~ 1.

Region (2), which contains decoupled and infalling material, starts roughly where the linear extrapolated density contrast is of order 1. Region (2) consists of material that has gone past turnaround and is infalling for the first time, but is sufficiently far from virial radius that there is no shell crossing occurring, only infall. The typical densities in this region range from 5-100 $\times\rho_{crit}$.

In Region (3), material is falling inwards, encountering inner shells that are expanding, or recollapsing; this is the shell-crossing region. Some of the shells are falling in for the first time; others may have undergone one or more oscillations but have not relaxed. It is well characterized by the scaling solutions of Gott (1975), and Gunn (1977), for which the slope of the density profile is a function of the ambient Ω_{matter}, with steeper slopes expected for smaller Ω_{matter}. In these models, critical density Universe produces halos with slopes of 2.25. Fillmore & Goldreich (1984) adopt a power law initial density profile and use a better dynamical approximation for treating the shells past the turnaround, leading to final profile slopes from $\rho \propto r^{-2.25}$ to $\rho \propto r^{-2}$. The typical densities in this region are about $100 - 500 \times \rho_{crit}$, and since $t_{orbital} \sim H_0^{-1}\sqrt{8}\,\pi[\rho/\rho_{crit}]^{-1/2}$ (or, for Einstein-de Sitter, $t_{orbital}/t_0 \sim 13.5[\rho/\rho_{crit}]^{-1/2}$) a typical particle in this region has completed at least one passage through the halo. Results of RG87 show that the density slopes at density contrasts of 100 are about 2.

In Region (4), virialization is well underway or is complete. Many analytical solutions in regions (1)-(3) ignore non-radial motions of particles; all orbits are assumed to be purely radial. This is probably a tolerable approximation for these regions. However, the approximation most definitely breaks down in the virialized central region of the halo, Region (4). Though Gott (1975), Gunn (1977), and Fillmore & Goldreich (1984) argue that their solutions apply to the virialized regions, this is not the case. Even in very smooth initial halos, particles will have some non-zero tangential velocities. These will become increasingly important as particles start falling towards the center of the halo. For a particle falling towards a centrally condensed mass, the radial velocity $v_{rad} \propto r^b$, where $b \geq -1/2$, with the exact value depending on the density distribution. The particle's angular momentum $r\ v_{tan}$, stays constant. As a result, $v_{tan}/v_{rad} \propto r^c$, where $c \leq -1/2$. Thus, tangential velocities always increase as particles fall inward. The calculations carried out in RG87 demonstrate that non-radial motions are very important in determining the outcome in this region. Non-radial motions give particles angular momentum, which prevents them from penetrating to the very center of the halo. This picture is supported by the recent work of Avila-Reese, Firmani & Hernandez (1998), Subramanian, Cen & Ostriker (1999) and Hozumi, Burkert & Fujiwara (2000), among others. For example, Subramanian *et al.* apply the collisionless Boltzmann equation to self-similar halo collapse to show that tangential velocities are necessary to attain central slopes shallower than 2. Hozumi *et al.* start with a power law density

profile and an initial v_{tan}/v_{rad} ratio and integrate the collisionless Boltzmann equation to arrive at the final phase-space density distribution of the halo. Hozumi *et al.* and others stress the importance of the initial distribution of radial vs. tangential velocities in the halo in determining the final profile of the central region of the halo.

The rates at which matter in regions (1), (2), (3) and (4) makes its way towards the center of the halo are different, reflecting the different types of dynamical processes going on. Therefore one should not expect a single density profile power law index to hold throughout the halo. In fact, all analyses that do not explicitly assume that power law profiles hold over a wide range of radii, find that profile slope does change with radius.

The dynamical process described above, that of accretion of mass from an expanding background and growth of structures from inside out, is called the secondary infall model (SIM). The assumptions used in the analytical implementation of SIMs were highly idealized in the 1970's, but have become more realistic in the recent years. For example, early models started with a δ-function or power law seed structure, and assumed purely radial particle motions and self-similar collapse, while more recent models relax all these assumptions. Table 1 summarizes some of the key SIM papers, and documents how the model assumptions have changed over time. An underlined item in Table 1 means that the corresponding paper was the first published use of that particular assumption (to the best of our knowledge).

SIM models were first explored in detail by Gunn & Gott (1972, GG72) who studied the evolution of a spherically symmetric halo up to the time of the maximum expansion. Gunn (1977, G77) followed the evolution of halos past the maximum expansion and into the shell-crossing regime. This paper introduced the use of adiabatic invariants: for self-similar radial collapse radial momentum is equivalent to $r \cdot m(r)$, where $m(r)$ is the mass enclosed within r. Fillmore and Goldreich (1974, FG84) further explored the dynamics of self-similar halo collapse, using a power law as the initial density profile. Zaroubi & Hoffman (1993, ZH93) refined the FG84 collapse calculations, by improving the estimation of the collapse factor of shells, i.e. the ratio of the shell's radius of maximum expansion and its asymptotic radius. Hoffman and Shaham (1985) used the two-point correlation function as a more realistic approximation to the initial density profile of halos. However, the radial shape of the typical *overdense* regions, i.e. peaks in the density field is steeper than the correlation function. Ryden & Gunn (1987) were the first to adopt peaks in the density field as the density profile of the proto-halos. RG87 were also the first to relax the assumption of purely radial self-similar collapse by including non-radial motions arising from secondary perturbations in the halo. Inclusion of non-radial motions required an additional adiabatic invariant; RG87's model conserves angular and radial momenta of each shell throughout the collapse. Avila-Reese *et al.* (1998) differs from most other works because their halos are assembled

through a series of discrete merger episodes, described by mass aggregation histories (MAH), which are generated from the Gaussian fluctuation field. Their dark matter particles are endowed with "thermal motions" resulting in non-radial velocities. Nusser (2000) tried two different analytical schemes for non-radial velocities in his halos, and concluded that angular momentum is most effective when added to a particle at the time of maximum expansion. Most of the SIM treatments assume that any given halo is completely isolated and so continues to accrete mass indefinitely, however Lokas (2000) argue that mass can be accreted only from a finite sphere, whose radius is 1/2 of the typical peak-to-peak separation. This results in the steepening of the outer density profile of the final halo. The last column in Table 1 states whether the final virialized density profile is a power law or not. All non-power law profiles have a 'concave' shape in the log-log plane.

Several of the papers listed in Table 1, as well as other works (e.g. Del Popolo *et al.* 2002, Hiotelis 2002, Kull 1999, Lokas & Hoffman 2000) compared their results to those of N-body simulations. In most cases they found their final profiles to be similar to NFW empirical fit, in particular, analytically generated halos possess central density cusps. In contrast, our density profiles, which we describe in Section 4, often have small flat density cores. This difference probably arises from the different methods used to generate the angular momenta of particles. We assume that angular momenta arise from the random secondary perturbations, and derive their magnitude in a self-consistent fashion from the same fluctuation power spectrum that generates the primary peak. All other analytical treatments use simple prescriptions to obtain angular momenta of particles as a function of radius, for example, $L^2 \propto M(<r)\,r$.

3. A brief summary of the Ryden & Gunn 1987 method

Our halo formation formalism builds upon the powerful analytical method introduced by Ryden & Gunn (1987), which allows one to track the evolution of dark matter halos in all four regions discussed in Section 2, while accounting for the effects of non-radial motions and shell crossing. In this Section we summarize the key elements of the original RG87 method; our refinements and extensions are discussed in Section 4. All the technical details are relegated to the Appendix.

In most popular cosmological scenarios the density field soon after recombination can be represented by a Gaussian random field. The amplitude of density fluctuations at that early time is very small, $\sim 10^{-5} - 10^{-4}$. If the initial spectrum is close to Harrison-Zel'dovich then the early evolution of the density field is very well described by linear theory, where, in the Einstein-de Sitter case the amplitude of perturbations grows as $\delta\rho/\rho \propto a(t) \propto t^{2/3}$, i.e. our Region (1). High density contrast peaks in the field will eventually achieve overden-

sities of order 1 and enter a non-linear stage of evolution. These peaks will then collapse to form bound structures. We start with one of these peaks, and, for simplicity take it to be spherically symmetric. The peak is divided into a very small central core and many spherically symmetric concentric mass shells, each labeled by its initial comoving distance from the center, x. Each shell's evolution is divided into two stages. Initially a shell expands with the Hubble flow, but with a slight deceleration arising from the central mass concentration. Eventually the shell's outward radial velocity decreases to zero, after which the shell collapses, by some distance, back towards the center of the halo. The dividing moment is called the turn-around, and at any given time corresponds to the line dividing Regions (1) and (2). In a halo with a declining density profile the turn-around happens at progressively later cosmic times for shells at greater distances from the center.

In reality, the initial density peak will not be smooth, but will instead be sprinkled with many smaller scale positive and negative perturbations that arise from the same Gaussian random field that gave rise to the main peak. These secondary perturbations will perturb the motion of the dark matter particles from their otherwise purely radial orbits.

In the early part of the evolution of the halo most of the shells are still expanding. During this time secondary perturbations grow, and so does the acceleration, the velocity, and the displacement contributed by these perturbations to the particles in the shell. Because the secondary peaks are randomly distributed within the halo, they displace the dark matter particles in random directions from their original positions. This can be visualized as a shell having an internal velocity dispersion, resulting in a 'puffy' shell. If we concentrate on a single particle, its orbit, viewed from the rest frame of the parent shell, will oscillate between an inner and an outer radius of that shell (i.e. peri- and apocenter). In general, this orbit will not be closed and will resemble a rosette. A time averaged picture of one particle's orbit in this scenario will be identical to a single-moment snapshot of all the particles in a shell[3].

In a real situation, the puffiness of any given shell will gradually increase as the shell expands away from the halo's center, and the influence of the secondary peaks grows, but for simplicity, our calculations assume that each shell stays dynamically cold and spatially thin during the expansion, and then puffs up instantly as it reaches turnaround. In other words, as long as a given shell is expanding its dark matter particles' positions and velocities are not corrected for the effects of secondary perturbations; it is assumed that during this relatively orderly evolutionary stage the effects of random perturbations are small compared to what they will be later when the halo starts to collapse. So, the contributions are evaluated analytically but are not imparted to the shell until it reaches turnaround. Furthermore,

[3]Note that in the rest of the paper we use the words 'shells' and 'particles' interchangeably.

only the velocities of dark matter particles are corrected; the positions are left unchanged, so in our halos the puffiness of the shells refers to their dynamical state, not to the spatial distribution of their dark matter particles.

At turnaround, every particles' kinetic energy is augmented by the additional velocity component, $\Delta\mathbf{v}_{\rm rms}(x)$, the rms value of the accumulated effect of secondary perturbations, which is a function of radial position in the halo. The three spatial directions are statistically equivalent as far as random velocities are concerned, so 1/3 of the total amplitude of $|\Delta\mathbf{v}_{\rm rms}(x)|^2$ goes to each of the three orthogonal directions. Instead of having $\Delta\mathbf{v}$ be defined uniquely by x, and dividing the amplitude equally among the three orthogonal directions, as was done in the original RG87 method, our formalism implements a distribution of velocity values at a given x (using the same $\Delta\mathbf{v}_{\rm rms}(x)$ as before), and picks the orientation of the velocity vector randomly, thereby better approximating the dark matter velocity structure of real halos.

As every additional shell reaches its turnaround radius and falls in, it overlaps a number of shells that have already fallen, all of which have their own peri- and apocenters. This is shell-crossing. The gravitational potential of the halo changes with every additional shell falling in, and has to be recalculated at every step. This means that the shells' orbits that overlap the newly fallen shell also have to be recalculated, keeping their angular and radial momenta fixed throughout the collapse. This process of shell readjustment goes on until the present cosmic time is reached.

4. Halo density profiles

In this Section we describe the formation of dark matter halos via our method. We start with the adopted structure of the proto-halos, and in Section 4.2 describe how our formalism has been extended from RG87.

4.1. The initial set-up

In the present paper we retain many features of the RG87 method, including the Einstein-de Sitter model. We assume an Einstein-de Sitter background cosmology instead of using a more popular flat, low density universe because we are most interested in the dynamics and spatial distribution of matter in regions where the density is well in excess of critical, by 1-5 orders of magnitude. In such dense regions the global value of Ω_{matter} should not matter much.

We use the standard CDM power spectrum, i.e. the scale-invariant Harrison-Zel'dovich $P(k) \propto k$ form. The transfer function that describes the transition of the $P(k)$ through the matter-radiation equality epoch was taken from Bardeen *et al.* (1996). Instead of RG87's $H_0 = 75$ km s^{-1}Mpc^{-1} we use $H_0 = 50$ km s^{-1}Mpc^{-1} which corresponds to standard CDM. The spectrum is normalized such that rms fluctuations in Gaussian smoothed spheres[4] of radius $5h^{-1}$Mpc are 0.5, in agreement with several recent determinations that estimate $\Omega^{0.5...0.6}\sigma_8 = 0.5$ (Eke *et al.* 1996; Mellier *et al.* 2001).

The smallest scales considered here are set by the filtering scale l_0, such that

$$P_s(k) = P(k)e^{-k^2 l_0^2}. \tag{1}$$

For consistency, the size of the unresolved core of each dark matter halo is set to $M_{core} \sim (2\pi)^{3/2}\rho_{crit}l_0^3$. We use $M_{core} = 10^6 M_\odot$, corresponding $l_0 = 10$ kpc. The shape of the core is assumed to be singular isothermal with an outer sharp cutoff at $r_{core} \sim 5$ kpc. The exact shape of the core does not matter since it is very small, comprising $\sim 10^{-4} - 10^{-5}$ of the total mass of a typical halo considered here. (Section A.5 contains further discussion of the halo's core.) Note that because the spectrum is filtered below l_0, smaller scale secondary perturbations are not included in the calculations. The mathematical details of the halo formation formalism are described in the Appendix.

4.2. Generating final virialized halos

We now describe our procedure for generating virialized dark matter halos. In a real halo, particles of a given shell will have a range of random velocities arising from the secondary perturbations. The RG87 formalism allows us to calculate the rms value, $|\Delta\mathbf{v}_{\rm rms}(x)|$ of these random velocities as a function of radius in the halo. RG87 assume that every particle in a given shell has the same $\Delta\mathbf{v}$ value, equal to the rms value (Section 3). We improve upon their method by allowing shells to have a *distribution* of velocities. The halo is broken up into a very large number of shells, and for each shell we pick a random value for $|\Delta\mathbf{v}|$ from a Maxwell-Boltzmann distribution of the appropriate rms half-width. Furthermore, instead of dividing $|\Delta\mathbf{v}|^2$ equally among three spatial directions, as in RG87, we pick a random orientation for the velocity vector $\Delta\mathbf{v}$ for each shell. The halo is then evolved in time using the procedure described in Section A.5.

[4]Note that a Gaussian window of radius $5h^{-1}$Mpc contains the same volume as a top-hat window of radius $8h^{-1}$Mpc.

Note that in our halos two adjacent shells can have very different velocities and orientations of the $\Delta\mathbf{v}$ vector. This is analogous to a real halo, where two nearby dark matter particles can have different random velocities, because they have been affected by a spatially varying field of secondary perturbations. To approximate a real halo, our halos are modeled with a very large number of shells. If the number of shells is not sufficient, then the resulting halo will have an uneven density distribution, with discontinuous jumps in density: some shells' pericenters will be close to halo's center and so will have their mass distributed over a wide range in radii, while other shells will be restricted by large angular momentum and will have their mass piled up in a narrow range of radii. So, two halos with the same input $\Delta\mathbf{v}_{\rm rms}(x)$ parameters can have somewhat different virialized profiles, especially in the inner halo regions. In other words, there will be a scatter in final halo properties. To obtain the average, or typical halo, two approaches can be used: (1) Generate n halos each having m shells, and then obtain the 'average' halo, which will then have a smooth density profile. (2) Generate one halo with $n \times m$ shells. The single final halo has a smooth density profile, because the very large number of shells smears out irregularities. Both of these approaches give the same results in terms of final halo properties, and serve as a test of the robustness of the method in view of the randomness of shells' $\Delta\mathbf{v}$ magnitude and orientation. All profiles in the figures presented in this paper were generated using either (1) or (2).

4.3. The standard reference case

In this paper we consider a range of initial parameters and their effect on the final virialized halos, focusing on different slopes and filtering scales for the primordial matter power spectrum. As a baseline, we generate a halo using 'standard' assumptions, which will be used as a 'reference' halo for later results. The reference halo starts out as a $3\,\sigma$ peak in the density fluctuation field of standard CDM spectrum, which has been filtered with a fixed l_0 smoothing scale ($l_0 = 10$ kpc, see Section 4.1) The virial radius of our reference halo at the present epoch is $R_{vir} = 0.23$ Mpc, and the mass contained within that virial radius is $M = 6.75 \times 10^{11} M_\odot$. The solid lines in all four panels of Fig. 1 represent the standard reference halo.

For comparison, we generate halos with masses above and below that of the reference halo. To generate these, we start with the same $P(k)$, smoothed on the same l_0 scale as before, but choose peaks of different heights, or σ's in the initial density fluctuation field. An initial $2\,\sigma$ peak collapses to a halo of final virialized mass $M = 3.5 \times 10^{10} M_\odot$, and a $M = 2.7 \times 10^{12} M_\odot$ halo forms from a $4\,\sigma$ peak. Higher peaks in the initial density field start collapsing earlier, and end up as more massive and more concentrated halos. This trend can

be seen in the upper left panel of Fig. 1. Because our halos are isolated (i.e. their formation does not involve major mergers which can change the halo's formation history in a stochastic way) there exists a one-to-one relation (for a fixed smoothing scale) between the height of the primordial peak, the epoch of collapse, the virial mass and the central concentration of halos produced in our formalism. We will discuss the origin of these trends in Section 5.5.

Note that our halos have flat density cores at center: in the case of the $M = 6.75 \times 10^{11} M_{\odot}$ reference halo the core is very small, $\sim 10^{-3}\, R_{vir}$. For the $M = 3.5 \times 10^{10} M_{\odot}$ the core is $\sim 0.025\, R_{vir}$, however in both cases the physical extent is roughly the same, ~ 1 kpc, smaller than are seen in most dwarf galaxies.

The upper right panel of Fig. 1 plots density profiles divided by a density profile with a slope of $\alpha = 2$, the slope that would result in a flat rotation curve. The part of the halo where the density profile has slope $\alpha = 2$ is flat in this plot. The differences between NFW of concentration parameter $c = 10$ (dot-dash curve) and our halos is clearly visible: our halo's slope changes slowly within the virial radius, whereas the NFW profiles change slope rapidly from $\alpha = 1$ to $\alpha = 3$ at the characteristic radius, $r_s = R_{vir}/c$.

The lower right panel casts the results in the form of the rotation curves, with the horizontal axis plotted linearly to facilitate comparison with observations. More massive galaxy halos tend to be more centrally concentrated, and have flatter rotation curves. Less massive halos are less concentrated, and have slowly rising rotation curves. In general our rotation curves tend to be approximately flat, because the density profile slope is close to $\alpha = 2$ in the region between 0.1 and 1 R_{vir}. In contrast, NFW rotation curves rise very steeply, a property which requires NFW fits to dwarf galaxy rotation curves to have very low concentration parameters (see van den Bosch & Swaters 2001), in fact, too low compared to the N-body predictions.

The lower left panel shows histograms of the distribution of specific angular momentum (SAM) of dark matter within the virial radius. In principle, there are two sources of angular momentum of collisionless dark matter: (i) bulk streaming motions, and (ii) random tangential motions. The first arises due to tidal torques experienced by proto-halos, and is usually quantified as a dimensionless spin parameter λ (Peebles 1969). Our halos do not have angular momentum of Type (i), only of Type (ii), so the net *vector* sum of angular momentum in our halos is zero. Because dark matter is assumed to be collisionless, it is the sum of the *magnitudes* of angular momenta of particles that is relevant for the dynamics, not the vector sum. In all the following discussions angular momentum will mean Type (ii) angular momentum.

The two smooth curves in the lower left panel of Fig. 1 are SAM distributions of dark

matter halos in N-body simulations, taken from van den Bosch *et al.* (2002), who present properties of 20 numerically simulated halos. This angular momentum is the sum total of streaming and random motions of dark matter particles, i.e. Type (i) and (ii) combined. Most of the SAM distributions taken from van den Bosch *et al.* tend to resemble the steeper of the two curves shown in Fig. 1, halo #170. Halo #081 has the shallowest of their SAM distributions. The plot shows that most halos generated using our technique have more angular momentum than typical N-body halos, even without the inclusion of Type (i) angular momentum from tidal torques. This is consistent with our halos having more extended mass distributions than NFW halos. We will return to this issue of angular momentum again in Section 4.4.

The properties of individual shells in virialized reference halos are presented in Fig. 2. The solid dots in top panels are the peri- and apocenters of shells, plotted as a function of their initial, pre-collapse, comoving location in the halo, x. As expected, there is significant scatter in properties of individual particles, since their $\Delta\mathbf{v}$'s were picked randomly from a distribution. The solid lines are averages over shells in many halos. (Dashed lines represent halos considered later, in Section 4.6.) The average orbit eccentricity is approximately constant within the virialized halo, changing only from $\langle r_{peri}/r_{apo}\rangle \approx 0.3$ at R_{vir} to 0.35 at $0.01\,R_{vir}$, as orbits become more circular close to center. The constancy of r_{peri}/r_{apo} was predicted by Nusser (2001) for halos with adiabatically varying potentials, and power law radial profiles. It is not entirely surprising that our method, which conserves adiabatic invariants, but does not insist on power laws density profiles, yields roughly constant $\langle r_{peri}/r_{apo}\rangle$ ratios. It is more surprising that very high resolution N-body simulations described in Ghigna *et al.* (1998) also produce constant $\langle r_{peri}/r_{apo}\rangle$ (≈ 0.2) ratios of dark matter particles in virialized halos. This constancy of $\langle r_{peri}/r_{apo}\rangle$ throughout the halo could suggest that the adiabatic approximation is largely valid for halos generated in N-body simulations (see also Jesseit *et al.* 2002).

The solid points in the lower panels of Fig. 2 plot the angular and radial momenta of individual particles in virialized halos. Each particle's j_θ and j_r are assumed to be constant throughout the collapse. The radial momentum, j_r and angular momentum j_θ are nearly equal The solid lines are averages of these momenta, taken over shells in many halos.

Before we go on, we note that the reference halo described in this section would have looked somewhat different had we used the original RG87 method, which applies the rms value of random velocities, $\Delta\mathbf{v}_{\rm rms}(x)$ to particles in each shell. Using a *distribution* of $\Delta\mathbf{v}$ at every x, as we do here, means that some fraction of particles acquire very small $\Delta\mathbf{v}$'s and j_θ's, and hence have nearly radial orbits. These orbits steepen the density profiles somewhat, especially in the inner halo. However, there is almost no change in density profile at larger

radii.

4.4. Comparison with NFW profiles

Figure 1 shows that halos generated using our method are different in character from the profiles predicted by numerical simulations, like those of NFW. This result is not surprising since the types of evolution that numerical N-body and our halos undergo are rather different: the former are produced as a cumulative result of many minor and major mergers of smaller sub-halos, while the latter are the product of quiescent accretion of lumpy matter onto the primary halo. The difference between the final virialized halos is best illustrated by the top two panels: within the virial radius the log-log density slope changes gradually from around $\alpha \sim 0$ to $\alpha \sim 2$. NFW profiles, on the other hand, have a characteristic scale-length, equal to $0.1\,R_{vir}$ in this case, beyond which the density profile slope steepens, so that much of the mass is piled up within 10% of the virial radius. This pile up is also reflected in the differences of the two angular momentum distributions, shown in the lower left panel of Fig. 1. The density and SAM distribution plots suggest that compared to NFW, the parts of our halos that lie between ~ 0.1 and $\sim 1\,R_{vir}$ retain more angular momentum.

To further explore the relation between our halos and NFW we perform the following experiment. We attempt to artificially modify the conditions within our halos, such that resulting halos resemble NFW. Figure 3 shows two halos: the solid line is the reference halo, while the dashed line represents a halo that was obtained by using same parameters as for the reference halo with one exception. For shells with initial comoving radii $x = 0.35 \rightarrow 1.3$ Mpc we have arbitrarily reduced the amplitude of all random velocities, $|\Delta\mathbf{v}|$ by a factor of 2. How does the initial comoving $x = 0.35 \rightarrow 1.3$ Mpc radius range translate into the present day particle location within the virialised halo? A shell that started out in the primordial halo at a comoving radius of $x = 0.35$ Mpc has settled to a present day configuration with apo- and pericenters at ~ 0.033 Mpc and ~ 0.012 Mpc, respectively. Similarly, a shell originally at a comoving radius of $x = 1.3$ Mpc has at the present epoch apo- and pericenters roughly equal to 0.7 Mpc and 0.18 Mpc. The $x = 0.35 \rightarrow 1.3$ Mpc range, and the factor of 2 reduction in random velocities were selected by trial and error. Note that we did not aim to reproduce an NFW profile *exactly*; the key feature that we wanted to emulate was the location of the break in the density profile, which occurs where $\alpha \approx 2$, at $r \lesssim 0.1 R_{vir}$ in the NFW halo.

The corresponding change in angular momentum distribution is seen in the lower left panel of Fig. 3. The SAM distribution of the NFW-like halo (dashed histogram) is more centrally concentrated than the SAM distribution of the reference halo (solid histogram), and is closer to those of typical halos emerging from numerical simulations (smooth lines).

The experiment that produced NFW-like halo suggests that compared to an isolated halo undergoing only quiescent accretion and minor mergers (like our halos), halos in N-body simulations lose a considerable amount of angular momentum between 0.1 and 1 R_{vir}. Since virialization proceeds from inside out, this means that the angular momentum loss takes place during the later stages of the halos' evolution, rather then very early on. In fact, several authors have noted that N-body generated dark matter halos have too little angular momentum compared to the halos of real disk galaxies, possibly because it was lost during repeated collisions through dynamical friction or other mechanisms (van den Bosch *et al.* 2002; Navarro & Steinmetz 2000). This problem is sometimes referred to as the angular momentum catastrophe. We suggest that halos formed via our method are closer in character to the real observed halos of spiral and dwarf galaxies, than are the N-body generated halos. The fact that thin extended spiral disks appear to be common in the Universe further supports our hypothesis, as it implies that quiescent formation histories are realistic, at least for some galaxies.

4.5. Tilting the power spectrum

A purely scale-invariant Harrison-Zel'dovich matter spectrum has the shape $P(k) \propto k^n$, where $k = 1$. However, inflation, the most popular scenario for generating scale-invariant spectra is more likely to give rise to slightly 'reddish' spectra, with $n \lesssim 1$, since exponential Hubble expansion slowed down as time advanced. Values of n below 1 have been considered recently in the literature, for example, by Zentner & Bullock (2002), as a possible solution to the central density problem of galaxies. Motivated by these considerations, we tried $P(k)$ with $n = 0.9$. The resulting halo density profiles are only slightly shallower than those shown in Fig. 1, so we do not show them here. Spectral index value smaller than 0.9 would produce noticeably shallower density profiles, but given the constraints on n from the Cosmic Microwave Background (Spergel *et al.* 2003, Jaffe *et al.* 2001) and the clustering of Lyman-α clouds (Croft & Gastanaga 1998), n is unlikely to be smaller about 0.9.

4.6. Filtering the power spectrum

Another physically motivated modification of the primordial power spectrum is filtering. Filtering the power spectrum, or, equivalently, smoothing the density field on a given scale is meant to mimic the effect of a warm dark matter particle, whose mass can be related to the filtering scale, r_f. Our choice of $r_f = 0.1$ Mpc is comparable to those used by other authors (Bode *et al.* 2001, Knebe *et al.* 2002). We make no attempt to motivate the exact choice

of the value of r_f starting from the mass of a hypothetical dark matter particle; instead we take the emperical approach and adopt filtering scales that are large enough to produce noticeable results, and are at the same time small enough so that proto-halo peaks of low mass galaxies are not completely erased.

We smooth the power spectrum with a Gaussian filter of variable size r_f,

$$P_f(k) = P_s(k)e^{-k^2 r_f^2}, \tag{2}$$

and show the resulting halos in Fig. 4. Filtering reduces the central densities of halos by a factor of $\lesssim$10, producing central cores of a few kpc in extent. Similar findings are reported by, for example, Avila-Reese *et al.* (2001), who find that filtering the mass power spectra in their N-body simulations produces halos of lower central concentration. A quantitative explanation of why we get cores is discussed in Section 5.5. The SAM distribution of all the material within the virial radius is very similar to that in Fig. 1, reflecting the fact that only the central parts of halos are affected by filtering.

4.7. Changing the shape of the velocity ellipsoid

So far we have assumed that the velocity vectors arising from secondary perturbations are randomly oriented. However, one could conceive of a process that would not alter the magnitudes of these velocities, but orient them preferentially tangentially with respect to the center of the halo, thereby flattening the shape of the velocity ellipsoid.

Specifically, we do the following. Every $\Delta\mathbf{v}$ vector is decomposed into *two* components: the radial (with respect to the center of the halo) and the tangential. The latter combines θ and ϕ directions of the usual spherical coordinate system. The tangential components of $\Delta\mathbf{v}$ vectors are distributed uniformly over the 2π radians of the tangential plane.

Let the angle between the tangential plane and $\Delta\mathbf{v}$ vector be ζ. To make a non-isotropic velocity ellipsoid, we keep the magnitudes $|\Delta\mathbf{v}|$ the same, but restrict the orientation of $\Delta\mathbf{v}$ to lie between angles $+\zeta_0$ and $-\zeta_0$. Within the range bounded by $\pm\zeta_0$ the orientations of $\Delta\mathbf{v}$ vectors are uniformly distributed. If $\zeta_0 = 90^\circ$ there is no restriction on the orientation of $\Delta\mathbf{v}$'s, whereas if $\zeta_0 = 0^\circ$ only tangentially oriented vectors are allowed.

To explore the effects of a non-isotropic velocity ellipsoids we set ζ_0 to values $< 90^\circ$. Having $\zeta_0 < 90^\circ$ creates an additional angular momentum barrier for dark matter particles, and hence results in the formation of flat density cores. For $\zeta_o \sim 20^\circ - 50^\circ$ the final halo density profiles look similar to those in Fig. 4, so we do not show them here. Instead, we show that these halos are a good fit to the rotation curves of dark matter dominated dwarf

galaxies and low surface brightness galaxies (LSBs). The four LSBs in Fig. 5 were taken from the recent high-resolution data of de Blok & Bosma (2002). Of the 26 LSBs that are presented in that paper we picked the ones with high inclination angles, smooth rotation curves, and good agreement between HI, Hα, and optical data.

The dashed lines in Fig. 5 are the NFW profile fits to the last observed point (except in the case of NGC 5023, where we fit to a point at 4 kpc). The concentration parameter c was chosen to be consistent with the NFW predictions, in other words, each rotation curve had only one free parameter; c values vary between 13.5 and 17 for these four galaxies. The solid lines are our halos with tangentially oriented velocity ellipsoids: for NGC 1560 and 5023, $\zeta_0 = 50^\circ$ was used, while for NGC 5750 and 100, more flattened velocity ellipsoids were used, with $\zeta_0 = 20^\circ$. Aside from ζ_0, there is only one free parameter in our fits, the mass of the virialized halo. In the case of NGC 100 and 5023 NFW and our halos do equally well in reproducing the rotation curves, in NGC1560 our halo provides a better match to observations, and in the case of NGC5750 our halo is a considerably better fit than NFW. For NGC 5750, we also plot the profile of a halo whose velocity ellipsoid is spherically symmetric ($\zeta_0 = 90^\circ$); see dotted line in the upper left panel of Fig. 5. So even a halo with spherically symmetric random velocity distribution is a much better fit to low mass galaxies, like NGC 5750, than an NFW profile. Note that $r_f = 0.1$ Mpc halos (Section 4.6) with randomly oriented $\Delta\mathbf{v}$ vectors also provide a good fit to these LSB rotation curves.

5. Understanding the halos

5.1. An absolute upper limit on the steepness of the central cusp

While the original NFW papers and later work by Power *et al.* (2003) showed that the inner profile slope, $\rho \propto r^{-\alpha}$, is close to $\alpha = 1$, Moore *et al.* (1998), based on their high resolution simulations argued that central cusps of halos are better characterized by $\alpha \approx 1.4 - 1.6$. To shed some light on this unresolved issue, we ask, how steep can the central density cusp get?

First, we conducted an experiment: we arbitrarily changed the amplitude of random velocities imparted to dark matter particles, $|\Delta\mathbf{v}|$, by factors of 3, 10 and 100. Reducing (increasing) $|\Delta\mathbf{v}|$ amounts to reducing (increasing) the angular momentum. The results are shown in Fig. 6. With each reduction of the random velocities, the profiles get steeper at the center. This steepening is easy to understand qualitatively in terms of an angular momentum barrier. The central density is built up by shells whose pericenters are very close to the center of the halo. Particles with large angular momenta are prevented from

coming close to halo's center and contributing to the central density. This is clearly seen in the halo where $|\Delta\mathbf{v}|$ was increased by a factor of 3. Conversely, more material with low angular momentum results in steeper central cusps. However, no matter how much angular momentum is reduced, it seems to be impossible to produce profiles steeper than log-log slope of $\alpha = 2$ in the central parts of halos. We now explain why this is the *absolute* steepest slope that can be achieved at halos' centers.

Let us approximate the central region of the halo by $\rho(r) = \rho_0 r^{-\alpha}$, since a single power law is a good approximation for a limited range of radii. The potential at a point r in the sphere of this density profile is

$$\psi(r) = -4\pi G\rho_0\Big[-\frac{r^{2-\alpha}}{(3-\alpha)(2-\alpha)} + \frac{{r_\infty}^{2-\alpha}}{(2-\alpha)}\Big] \tag{3}$$

where r_∞ is the truncation radius of the halo. In this potential a particle's radial velocity is given by eq. A26:

$$v_{rad} = [2(E - \psi(r)) - (j_\theta/r)^2]^{1/2} \tag{4}$$

We now make two approximations in this expression for v_{rad}. First, the particle's total energy E can be assumed to be equal to its potential energy at apocenter. Its kinetic energy can be ignored because $v_{rad} = 0$, and v_{tan} attains its minimum value at this radius. So except for the nearly circular orbits, the total energy is $E = \psi(r_{apo})$. Second, for elongated orbits $j_\theta/r = v_{tan}$ is almost always smaller than v_{rad} (except at apo- and pericenters), because the latter includes random as well as bulk motions, while the former includes only random motions. Therefore we can assume that j_θ in eq. 4 is zero in most cases of interest, and in particular for those orbits which pass through the central cusp. Eq. 4 then becomes:

$$v_{rad}^2 = 2[\psi(r_{apo}) - \psi(r)] = 8\pi G\rho_0\Big[\frac{{r_{apo}}^{2-\alpha} - r^{2-\alpha}}{(3-\alpha)(2-\alpha)}\Big]. \tag{5}$$

The solid lines in Fig. 7 implement Eq. 5: they show how the radial velocity changes with the radial position, (r/r_{apo}) of the particle, for particles living in halos with different density profile slopes: $\alpha = 1.99, 1.9, 1.75, ...$ 0.5 (top to bottom). In general, v_{rad} increases as particles get closer to center, but then becomes nearly constant at very small radii.

For a single shell, the time spent within dr of r is inversely proportional to the shell's (or particle's) radial velocity. So the density a shell contributes at r is proportional to $(r^2\ v_{rad})^{-1}$. If the halo mass density at r is the sum of contributions of all shells that pass through r, and each shell is characterized by v_{rad}, then we must insist that $\rho(r) = \rho_0 r^{-\alpha} \propto (r^2\ v_{rad})^{-1}$, and so $v_{rad} \propto r^{\alpha-2}$. When this condition is applied to solid curves in Fig. 7 the only viable solutions that remain are marked by solid dots (one solution for each value of α). One readily sees that as the profile steepens towards $\alpha = 2$ the orbit shapes have to get progressively more

radial. To achieve $\alpha = 1.9$, r/r_{peri} must be nearly 100, and so r_{apo}/r_{peri} must exceed 100. Such radial orbits are hard to achieve since even the slightest amount of angular momentum will prevent these extreme orbit elongations. To attain $\alpha = 2$, r_{apo}/r_{peri} of orbits must be nearly infinite. Thus there is an absolute upper limit on the steepness of the density cusps in real halos.

This mechanism can be understood intuitively: as particles get close to their pericenters, their velocities increase, and so they spend less time close to the halo's center, and contribute little to central mass density. In other words, steepening up of the central cusp is a self-limiting process.

One may wonder why the mechanism just described does not impose an upper limit on the slope of density profiles far from center. The key difference is that at the center the density is built up by inner parts (pericenters) of outer shells alone. At positions in the halo other than the center, density is built up by a combination of apocenters of inner shells, pericenters of outer shells, and intermediate radii shells, so the situation is more complicated.

5.2. A practical upper limit on the steepness of the central cusp

While it is still uncertain whether the central cusp of numerically simulated halos is better approximated by $\rho \propto r^{-1}$ or $\rho \propto r^{-1.5}$, cusps steeper than $\alpha \approx 1.5$ are not typically seen in simulations. The model presented in Section 5.1 offers a possible explanation for this, i.e. it allows us to place a *realistic* upper limit on the steepness of cusps.

First, we compare the predictions of our analytic model, represented by solid dots in Fig. 7, to the data from the dark matter halos generated both with our semi-analytic method and with N-body techniques. The horizontal arrows in Fig. 7 represent data taken from our dark matter halos; the cross at (-0.70, 0.05) represents high resolution N-body halo of Ghigna *et al.* (1998). These data points were plotted as follows: the horizontal coordinate is $\log(r_{peri}/r_{apo})$ of orbits located around $0.01 - 0.05\ R_{vir}$, i.e. in the inner parts of halos. $\mathrm{Log}(r_{peri}/r_{apo})$ is the minimum value that $\log(r/r_{apo})$ can attain, so the arrow symbols signify that we are plotting lower limits on $\log(r/r_{apo})$. The vertical axis in Fig. 7 calls for the radial velocity of the particles near the central cusp. However, our model predicts a monotonic one-to-one correspondence between $\log(v_{rad})$ and α, represented by the dashed line in Fig. 7. So rather than measuring v_{rad} directly, we take the measured inner slope α and derive the value of v_{rad} that simultaneously solves the constraints given by Eq. 5 and by $v_{rad} \propto r^{\alpha-2}$.

The model predictions agree rather well with the 'observed' data points, and both indicate that steeper inner slopes require progressively more radial orbits. Fig. 7 indicates

that there is a 'break' in this relation, at around $\alpha \sim 1.6$. Now, radial orbits imply that the particles have small angular momenta. In a realistic setting, any number of numerical effects, ranging from sensitivity of equations of motion to round-off errors, the stiffness of the integrators, to the discreteness effects such as two-body heating, can increase the angular momenta of particles that otherwise would be on highly radial orbits. This increase in j_θ will lead to an increase in $\log(r/r_{apo})$. For $\alpha \gtrsim 1.6$, $\log(r/r_{apo})$ is a very sensitive function of α, therefore even a small additional j_θ will quickly bring α to $\sim 1.5 - 1.7$, and hence lead to the flattening of the cusps. This can explain why cusps steeper than $\alpha \sim 1.6$ should be rare. To flatten the cusps beyond $\alpha \sim 1.5 - 1.7$ would require considerably rounder orbits, and so larger j_θ.

5.3. Why are the halo density profiles concave?

Figure 6 demonstrates why, in general, density profiles tend to be 'concave', that is, the log-log slope of density profiles steepens monotonically with distance away from center. First, consider a halo with negligible random velocities (dotted line in Fig. 6). Such halos have slopes $\alpha \approx 2$ over 2-3 decades in radius. The orbits of particles are quite radial, with material being able to reach almost to the center. Now imagine imparting a small amount of angular momentum to the shells' particles. The pericenter radii are very sensitive to j_θ. Increasing j_θ by a roughly constant factor increases the pericenters of most shells by a constant factor as well. This withdrawal of material has a disproportionately larger effect on the smaller volume inner regions of the halo, producing concave profile shapes. Increasing j_θ results in progressive shallowing of the slope towards the center of the halos. Figure 6 illustrates this steady shallowing: the increase in $|\Delta \mathbf{v}|$, and hence j_θ has the greatest impact on the inner density slope.

The limiting case of $\alpha = 2$ slope attained for pure radial motions has already been noticed in the literature, in particular by Avila-Reese *et al.* (1998) and Subramanian *et al.* (1999). These authors also note that introduction of angular momentum results in the shallowing of the central parts of halos. Avila-Reese et al. (2001) attain soft cores in halos after introducing significant thermal velocities. These results are in full agreement with our work. When we increase the amplitude of random motions, and hence angular momentum, the resulting halos develop large flat density cores, as illustrated by the short-dash line in Fig. 6.

5.4. A universal relation between r_{peri}/r_{apo} and j_θ/j_r

Even though the values of apocenters and pericenters and of angular and radial momenta vary substantially from shell to shell within a given halo (see Fig. 2), and even more so between different types of halos, the relation between r_{peri}/r_{apo} and j_θ/j_r is very tight for shells in all halos. This is illustrated in Fig. 8. The upper right island of points are particles in the reference halo (Section 4.3), while the lower left set of points were drawn from a halo whose random velocities were reduced by a factor of 100 (dotted line in Fig. 6). The dispersion in the relation is always small, typically a factor of 1.5. The relation is tight because, as we show below, it is determined by the shape of the gravitational potential of the halo, which is relatively smooth. We can understand the shape of this relation by considering two limits: orbits with small angular momenta, and orbits with large angular momenta.

We first consider the small angular momentum limit. As before (see Section 5.1), we approximate the density profile over a limited range of radii (between apocenter and pericenter of a given orbit) by a power law: $\rho(r) \propto r^{-\alpha}$. As explained in Section 5.1, the particle's energy is given by $\psi(r_{apo})$, with the potential given by eq. 3. At pericenter, $v_{rad} = 0$; applying this to eq. 4 we get:

$$\frac{j_\theta}{r_{peri}} = \left[\frac{8\pi G\rho_0}{(3-\alpha)(2-\alpha)}\, r_{apo}^{2-\alpha}\Big(1 - \Big[\frac{r_{peri}}{r_{apo}}\Big]^{2-\alpha}\Big)\right]^{1/2} \tag{6}$$

If j_θ is not too large, then the particle's radial velocity is given by eq. 5, and its radial momentum is

$$j_r = \int_{r_{peri}}^{r_{apo}} v_{rad}\, dr = \left[\frac{8\pi G\rho_0}{(3-\alpha)(2-\alpha)}\, r_{apo}^{2-\alpha}\right]^{1/2} \int_{r_{peri}}^{r_{apo}} \Big(1 - \Big[\frac{r}{r_{apo}}\Big]^{2-\alpha}\Big)^{1/2}\, dr. \tag{7}$$

Combining eqs. 6 and 7 we get,

$$\Big(\frac{r_{peri}}{r_{apo}}\Big)\Big/\Big(\frac{j_r}{j_\theta}\Big) = r_{apo}^{-1} \int_{r_{peri}}^{r_{apo}} \Big(1 - \Big[\frac{r}{r_{apo}}\Big]^{2-\alpha}\Big)^{1/2}\, dr \Big/ \Big(1 - \Big[\frac{r_{peri}}{r_{apo}}\Big]^{2-\alpha}\Big)^{1/2} \tag{8}$$

For a fixed value of α of less than 2, the right hand side is roughly constant; so j_θ/j_r is approximately proportional to r_{peri}/r_{apo} with a constant of proportionality that depends on α. The three solid lines in Fig. 8 were obtained using eq. 8, for $\alpha = 1.99$, 1 and 0.5 (starting from the top).

Equation 8 breaks down for shell orbits that are close to circular, because we neglected j_θ in estimating v_{rad}. So the solid lines in Fig. 8 cannot continue to hold true for more circular orbits. However, in the limit of circular orbits we have a simple relation: as j_θ/j_r

gets large, as it would for orbits approaching circular shape, r_{peri}/r_{apo} approaches 1, giving us a convergence point in the upper right corner of Fig. 8, whose location is independent of α.

All the data points from our halos conform to this model. The lower left set of points belong to a halo with a nearly constant $\alpha = 2$ density profile, and are clustered just below the corresponding model line. The upper right set of points belong to a halo whose density profile slope varies considerably with distance from center, and are scattered between the curves for $\alpha \sim 1$ and ~ 2. In fact, particle orbit parameters of any halo considered here would also trace out the same curve. For example, the halo designed to mimic the NFW halo (Section 4.4 and Fig. 3) obeys this relation, even though it was generated somewhat artificially, by removing some amount of angular momentum from outer shells. We argue that this relation between r_{peri}/r_{apo} and j_θ/j_r and its dependence on the slope of the density profile of the dark matter halo will continue to hold when the spherical symmetry condition is relaxed, i.e. for mildly triaxial mass distributions, because the derivation of the relation depends on the sphericity of the potential, which is always rounder than the corresponding mass distribution. We speculate that all *virialized* shells will obey this relation, regardless of how the halo reached virialization.

5.5. Initial $P(k)$ and shapes of virialized halos

From the experiments carried out in Section 4.5 and 4.6 we see that if the initial $P(k)$ is modified such that it has less power on small scales compared to the standard power spectrum, then the final virialized halos will have central density profiles that are shallower compared to the standard case of Section 4.3. For example, Fig. 4 illustrates that filtering the initial high-z power spectrum on the comoving scale of 0.1 Mpc results in shallow density cores. We argue that these characteristics can be traced back to a single cause: the dependence of the turn-around radius and collapse time on the interior average density in the pre-collapse halo.

The turn-around radius, r_{max}, and the time taken to reach r_{max}, both go inversely with the average density interior to the shell (eqs. A2 and A3). The density profiles of proto-halos are proportional to the correlation function and thus if small scale power in $P(k)$ is reduced, the central density of high-z proto-halos is lowered. Consequently, inner shells are able to expand further compared to the standard $P(k)$ case, and it takes them longer to do so. This further implies that shells will collapse and virialize later. (Note that the outermost shells are not affected, since the average interior density for distant shells is hardly different from that of the standard case.) We now discuss specific consequences of this.

(i) Displacement of particles: Since the inner shells now take longer to expand, secondary perturbations have a longer time to act on the dark matter particles. However, the perturbation power spectrum is truncated at short scales. These two effects partly cancel each other, but still result in a net increase in the final displacement of particles (eq. A18).

(ii) Random velocities of particles: The magnitude of the final rms random velocity, $|\Delta \mathbf{v}_{\rm rms}(x)|$ of eq. A21 is a product of the velocity growth factor, F_v, which describes the time evolution of random velocities, and the rms value of the initial acceleration, arising from secondary perturbations, eq. A17. The velocity growth factor is increased when there is less mass fluctuation power on small scales, because there is more time for the perturbations' effects to accumulate. At the same time, the rms value of the initial acceleration is somewhat decreased because there is less contribution to the integral in eq. A17 from power on small scales, due to the increase in particle displacements, as discussed in (i). Because of these two opposing effects, the magnitude of $|\Delta \mathbf{v}_{\rm rms}(x)|$ is only slightly increased.

(iii) Angular and radial momenta of particles: What matters most for the subsequent dynamics of the halo are the angular and radial momenta of dark matter particles in the inner shells. Despite the fact that $|\Delta \mathbf{v}_{\rm rms}(x)|$ is only somewhat increased, the momenta are increased significantly because of the increase in the turn-around radius, see eqs. A24 and A24. The bottom panels of Fig. 2 depict the change in momenta for halos formed from filtered initial power spectra (dashed line), as well as from the standard initial conditions (solid line). Increased j_θ prevents particles from coming close to the halo center (the upper panels of Fig. 2) thereby decreasing the central density.

The qualitative explanation given above, and especially the role of r_{max} and turn-around time in determining j_θ, also helps understand why more massive halos are more concentrated (Section 4.3) than less massive halos. Higher σ peaks (progenitors of more massive halos) have greater density contrasts at their center, and so shells do not expand far before beginning to collapse. This reduces j_θ, and allows halos to become more concentrated. We caution that this trend of increased central concentration as a function of mass applies only to halos that started out as peaks in the density field smoothed with a fixed l_0 scale. Our conclusions do not mean that, for example, clusters of galaxies will be very much more centrally concentrated than galaxies, since different smoothing scales would apply in the two cases.

This quantitative argument explains why halos formed through quiescent accretion of small sub-halos, with no major mergers, would retain some memory of the initial conditions, such as the shape of the power spectrum (also see Ryden 1988b).

6. Summary and Future Work

In this paper we used an analytic technique to explore dark matter halo formation of galaxy-mass halos. Our method is derived from Ryden & Gunn (1987) and assumes conservation of angular and radial momenta of halo shells, as the halo collapses and virializes. The important feature of the method is the inclusion of secondary perturbations, which lead to radial and tangential velocity dispersion of halo particles. The resulting angular momentum of the halo due to random tangential velocities makes collapse proceed in a fashion very different from the purely radial collapse considered in early analytical work. In contrast to other recent analytical works, our halos acquire angular momentum from secondary perturbations, whose magnitude is derived from the fluctuation power spectrum, in a self-consistent way. The slope, filtering, and normalization of the initial power spectrum can be specified as desired. We have improved upon the original RG87 formalism by allowing dark matter particles to have a range of random velocities, which vary in both magnitude and direction at any given radial location in the halo. This allows us to explore different halo formation scenarios which produce different velocity ellipsoids. As a result, we have gained a deeper understanding of the process of halo formation.

Our galaxy-mass halos formed under standard cold matter matter initial conditions differ from universal profiles found in Navarro *et al.* (NFW) and Moore *et al.* (1998) numerical N-body simulations. While the latter have a pronounced density profile slope change at about 10% of the virial radius, our halos exhibit a much more gradual slope change. Specifically, the double logarithmic density slope of our halos, steepens to $\alpha = 2$ at around the virial radius, whereas the numerical profiles' slopes are close to $\alpha = 3$ well within the virial radius. This difference results in our rotation curves being much flatter over a longer range in radii compared to the universal rotation curves. The specific angular momentum distribution of our halos is also different from those of numerical simulations; the former is more extended, consistent with the halo mass distribution being also more extended. Under standard initial conditions our halos develop small central density cores. However, if the velocity ellipsoid is made somewhat tangential then the resulting cores are large enough to reproduce rotation curves of LSB galaxies.

All in all, our halos appear to be a closer match to the halos of spiral and dwarf galaxies, than are N-body halos. This may indicate that the halos of real late-type disk galaxies undergo a formation scenario similar to the one depicted by our method, i.e. collapse proceeds through a quiescent accretion of lumpy material and minor mergers, rather than through a merger-driven formation process characteristic of fully hierarchical models.

Guided by the properties of our virialized halos generated from standard as well non-standard and 'experimental' initial conditions, and aided by a simple analytical model, we

were able to answer some general questions regarding halos. In particular, we show that the inner cusp slope cannot exceed $\alpha = 2$. Moreover, in any realistic setting, the cusp will be shallower than $\alpha \sim 1.5 - 1.7$. This is a promising explanation for why numerically simulated halos have central cusps in the range $\alpha \sim \ 1 - 1.5$. However, it is also possible that the central cusps are due to some lingering effects of numerical noise.

In spite of the large dispersion in properties of individual halo shells (apo- and peri-centers, radial and angular momenta), and the differences in shapes of halos formed from a range of initial $P(k)$ and endowed with various amount of random particle motions, all shells obey a tight relation between r_{peri}/r_{apo} and j_θ/j_r ratios. We derive this relation analytically, and speculate that because it relies mostly on the shape of the halo's potential, the relation is 'universal'. In other words, we expect that particles of any virialized halo, regardless of how it was assembled, will obey this relation. Finally, we explain why halos generated via our formalism, i.e. through quiescent accretion of mass, retain some memory of initial conditions, in particular, the shape of the primordial fluctuation power spectrum.

Though we understand halos formed via our method relatively well, and have gained some insight into the numerically generated N-body halos, we have yet to uncover the reason for one of the main features of NFW halo profiles: the rather abrupt change in slope at the characteristic radius, well within the virialized portion of the halo. A promising step in that direction is that we now know how to arrive at NFW profiles within our semi-analytical formalism. Compared to a quiescent accretion, numerically generated halos must have lost a considerable amount of their angular momentum in the outer parts, roughly between 0.1 and 1 R_{vir}, possibly through dynamical friction or other mechanisms.

As the next step in our work, we plan to extend our halo formation technique to include global tidal torques, axisymmetric collapse, and effects of mergers.

We would like to thank the anonymous referee for suggesting that we compare our halos' velocity rotation curves to those of the observed LSB and dwarf galaxies; this and other suggestions greatly improved the paper. AB is supported by an NSERC Discovery Grant. He also acknowledges the hospitality extended to him by the Canadian Institute for Theoretical Astrophysics during his tenure as a CITA Senior Fellow. JJD was partially supported through NSF grant AST-990862 and the Alfred P. Sloan Foundation.

A. A summary of RG87 method

Here we will describe, in detail, the analytical galaxy formation formalism developed by Ryden and Gunn (1987). Our presentation differs somewhat from theirs, but we would like to stress that everything presented in this Appendix is taken from RG87. We will often quote equation numbers to help the reader make the connection with their original work.

A.1. Initial set-up

Ryden and Gunn (1987) start with an Einstein-de Sitter $\Omega = 1$ universe model, and H_0 of 75 km s^{-1}Mpc^{-1}. They assume that the matter density is dominated by collisionless cold dark matter, CDM. The primordial spectrum of matter density perturbations is Harrison-Zel'dovich and the transfer function was taken from Appendix G of Bardeen *et al.* (1986). The post-recombination linear fluctuation spectrum, $P(k)$, is smoothed on comoving scales $l_0 = 120$ kpc, small compared to the linearized size of the galaxy, i.e. size of the galaxy *before collapse*. The smoothing scale corresponds to the mass of the central core of the halo, $M = (4\pi/3)\rho_0 l_0^3$, and is about $10^9 M_\odot$ for the above choice of l_0. The smoothed power spectrum is related to the unsmoothed one by, $P_s(k) = P(k)e^{-k^2 l_0^2/2}$, for a top-hat filter. The smoothed spectrum is then normalized such that the *rms* fluctuations in mass in top-hat spheres of radius $x_0 = 10$ Mpc are unity at the present time. The unsmoothed spectrum is not used from now on; all relevant quantities are derived using $P_s(k)$.

Galaxies form from high peaks in the density field, high enough so that they stand out above the 'noise' and dominate the infall dynamics of the surrounding matter. What is the mean excess density distribution around a peak? Density profile around particles located at the local maxima *and* minima of the density field is given by $\langle \frac{\delta\rho}{\rho}(x) \rangle = \langle \delta(x) \rangle = n\xi(x)/\xi(0)^{1/2}$ (Peebles 1984), where ξ is the two-point mass correlation function, and x is the comoving separation. Eliminating minima, the density excess around centers of local density peaks was derived by Bardeen *et al.* (1986), and is given by eq.(9) of RG87. The amplitude of any given peak is expressed in terms of its σ deviation, where $\sigma = \xi(0)^{1/2}$, and $\xi(0)$ is the zero lag value of the two-point function. Thus the central density contrast of an $n\sigma$ peak is $n\xi(0)^{1/2}$. Given that galaxies are rather common, they must have formed from peaks that are not very rare, say, 2-4 σ peaks. Density profiles for $n = 2, 3$, and 4 and plotted in Figure 9. Thin lines are density runs around maxima or minima, and are proportional to $\xi(x)$. Thick lines show $\delta_0(x)$, the initial excess density distribution around a peak linearly evolved to the present day. The density profile of an initial, pre-collapse halo, at early times, $\delta_i(x)$, is related to $\delta_0(x)$ by the linear growth factor: $\delta_i(x) = \delta_0(x)/(1 + z_i)$.

The reason why density profiles around peaks (thick lines in Fig. 9) are steeper than those around density extrema (thin lines) is easy to understand in a qualitative way. Around centers of peaks the density decreases with radius, around centers of valleys it rises. 'Subtracting' the contributions of the valleys from the overall correlation function we get the profiles of peaks, which would then have density dropping off faster with x than a correlation function. Now consider very high peaks in the density field: a disproportionately large fraction of particles reside in these, and because the correlation function is weighted by the square of the particle density the profile of the very high density peaks will be close to that of the correlation function.

The density profiles in Fig. 9 are not singular at center, but have roughly constant density cores. This is because smoothed power spectrum was used to produce $\xi(x)$ and hence $\delta_0(x)$.

So far we have a perfectly spherically symmetric initial density profile. However, the initial density peak will in general have a triaxial shape, leading to non-spherical collapse. The dynamics of the halo collapse are dictated by the potential, which, being a double integral over all space, is much rounder than the mass distribution. Therefore the effects of intrinsic triaxiality of initial density peaks are smaller than those due to the secondary perturbations, and so can be ignored. Furthermore, initial triaxiality is less severe in larger, 2-4 σ peaks (Bardeen *et al.* 1986), which are the subject of the present study. With this caveat the smooth part of our density peak is still described by RG87 eq.(9). The corresponding profiles (thick lines in Fig. 9) are the starting point of further calculations.

In addition to the smooth halo, RG87 consider contributions from the secondary perturbations which arise from the same Gaussian random field that gave rise to the main halo. The effects of the secondary perturbations on the dynamics and final profiles of halos are the main topic of their paper. Strictly speaking, the rms amplitude of secondary fluctuations is reduced close to the central peak because of the constrained nature of the field; for simplicity RG87 ignore this small effect.

The overall initial density profile, linearly evolved to the present day, can be written as,

$$\rho(\mathbf{x}) = \rho_0[1 + \delta_0(x)][1 + \epsilon_0(\mathbf{x})], \tag{A1}$$

where ρ_0 is the present day background density, density excess due to the main halo is $\delta_0(x)$, and is assumed to be spherically symmetric, and $\epsilon_0(\mathbf{x})$ is the density excess contributed by the random secondary perturbations.

The initial set-up is now complete; next we address the dynamics of halo collapse. The plan is as follows. In Sections A.2 and A.3 we consider the time evolution of $\delta(x)$ and $\epsilon(\mathbf{x})$, respectively, until shells reach turn-around radius; in Section A.4 we calculate

the acceleration, velocity, and displacement of the dark matter particles due to secondary perturbations $\epsilon(\mathbf{x})$; and in Section A.5 we follow the shells past the turn-around and through the non-linear process of shell-crossing, and describe how to arrive at the final, equilibrium state of the halo.

A.2. Evolution of $\delta(x)$ until turn-around

Let us divide the main smooth spherically symmetric halo, $\delta_0(x)$, into many concentric mass shells. Each shell is uniquely labeled by x, its initial comoving radius. The halo represents an upward departure from average background density, i.e. density interior to any shell is greater than critical at all times. In such cases the time evolution of a shell until it reaches turn-around is given by a set of parametric equations (Gunn & Gott 1972, Peebles 1980),

$$r(\theta) = \frac{1}{2} x \bar{\delta}_0^{-1} (1 - \cos\theta) \tag{A2}$$

$$t(\theta) = \frac{3}{4} t_0 \bar{\delta}_0^{-3/2} (\theta - \sin\theta), \tag{A3}$$

where r is particle's proper radius, t is cosmic time, and $\bar{\delta}_0(x)$ is the initial average fractional density excess inside the shell (eq.[13] of RG87),

$$\bar{\delta}_0(x) = \frac{3}{x^2} \int_0^x \delta_0(y)\, y^2\, dy, \tag{A4}$$

and t_0 is the present time. At very early times, when $\delta \approx 0$ at all radii, eqs. A2 and A3 reduce to $r(t) = x(t/t_0)^{2/3}$, which means that the proper radii of shells trace the evolution of the scale factor; at early times all shells grow at the same rate. Much later, shells begin to reach their maximum expansion radii. A given shell reaches its maximum radius, $r_{max}(x)$, at time $t_c(x)/2$ (half the collapse time) when its time parameter θ is equal to π. Prior to turn-around, i.e. when $\theta < \pi$ the expansion proceeds according to the equations above, and θ and t can be used interchangeably for any given shell. The mass of a shell, and the mass within a shell are constant; these relations, together with eqs. A2 and A3 can be used to compute the fractional overdensity for any shell, parameterized by its $\delta_0/\bar{\delta}_0$, at a cosmic time corresponding to θ, (eq.[23] of RG87):

$$\delta(\theta) + 1 = \frac{9(\theta - \sin\theta)^2}{2(1 - \cos\theta)^3} \left(1 + 3\Big[1 - \frac{\delta_0}{\bar{\delta}_0}\Big]\Big[1 - \frac{3\sin\theta(\theta - \sin\theta)}{2(1 - \cos\theta)^2}\Big] \right)^{-1}, \tag{A5}$$

This can be used to construct the density run of a halo at a fixed cosmic time t/t_0.

A.3. Evolution of $\epsilon(\mathbf{x})$ until turn-around

As the primary density peak grows, so do the secondary perturbations $\epsilon(\mathbf{x})$. The main peak is assumed to be immersed in a uniform background, therefore the dynamics of the halo particles are dominated by the main peak. In particular, the growth rate of $\epsilon(\mathbf{x}, t)$ is a function of the local density and the local tidal field, both due to the main peak. This can be intuitively understood by considering two extreme cases of secondary peaks, located in different regions of the main halo. First, consider a density perturbation close to the center of the halo. The mass distribution around it is roughly spherical, so that the peak will behave as if it were living in a Universe of a higher average density, and hence will experience a higher growth rate. If the secondary peak is exactly at the center of the main peak, tidal forces vanish and the growth rate is a function of local overdensity only, see eq.(32) of RG87.

Now consider another perturbation, located on the outskirts of the main peak. It will experience tidal forces arising from the very asymmetric distribution of mass around it: main density peak on one side, and average density field on the other. In a 2D or 3D situation these tidal forces would elongate the secondary peak inducing faster collapse along the shorter axis, leading to increased growth rate. Our case is spatially 1D, i.e. radial, so the tidal forces will stretch the perturbation equally in all directions, thereby decreasing the peak's density and reducing its growth rate.

In a statistical sense, the growth rate will depend on $\delta_0/\bar{\delta}_0$, or, equivalently, x, either of which can be used to parameterize the strength of the tidal field in a spherically symmetric halo. The final expression for the growth rate is given by (eq.[28] of RG87)

$$\epsilon(x,\theta) = \frac{\epsilon_0(x)}{\bar{\delta}_0} \frac{f_2(\theta)}{f_1(\theta) - [\delta_0(x)/\bar{\delta}_0(x)] f_2(\theta)}, \tag{A6}$$

where $\epsilon_0(x)$ is the amplitude of the initial perturbation, given by eq. A12, and f_1 and f_2 are functions of the 'time' parameter θ: $f_1(\theta) = 16 - 16\cos\theta + \sin^2\theta - 9\theta\sin\theta$, and $f_2(\theta) = 12 - 12\cos\theta + 3\sin^2\theta - 9\theta\sin\theta$. Thus the same average growth rate is shared by all perturbations at a given radial x. The growth proceed as follows. According to eq. A6, at early times $\epsilon(t) \propto t^{2/3}$, a standard linear growth result for Einstein-de Sitter, and is independent of the radial location of the peak. Later, centrally located peaks start to grow much faster than suggested by the linear predictions, while the growth rate of perturbations on the outskirts of the halo, where $\delta_0/\bar{\delta}_0 < 0.5$, fall somewhat below the linear growth rate (see Fig.6 of RG87). Note that the derivation of eq. A6 assumes that $\epsilon(x,\theta)$ averaged over all the secondary peaks within any given radius x is 0, $\bar{\epsilon}(x) = 0$; in other words secondary perturbations contain zero *net* mass.

A.4. Dark matter particle velocity and displacement at turn-around

As the halo expands at an ever decreasing rate, the randomly placed secondary density peaks within the halo grow (as described in the last section) and exert accelerations on the dark matter particles (as described in this section).

At any given time and proper position the random acceleration due to perturbation field $\epsilon(\mathbf{r})$ is given by (RG87 eq.[40]):

$$\mathbf{g}(\mathbf{r},t) = \mathbf{g}_{tot}(\mathbf{r},t) - \mathbf{g}_b(\mathbf{r},t) \approx G \int d^3r' \frac{\rho_b(\mathbf{r}',t)\epsilon(\mathbf{r},t)}{|\mathbf{r}'-\mathbf{r}|^3}(\mathbf{r}'-\mathbf{r}), \tag{A7}$$

which is an integral over all space, and $\rho_b(\mathbf{r},t) = \rho_0(t)[1+\delta(\mathbf{r},t)]$ is the background density due to the main halo, and is related to the total density given by eq. A1 by, $\rho(\mathbf{r},t) = \rho_b(\mathbf{r},t)[1+\epsilon(\mathbf{r},t)]$; $\rho_0(t)$ is the average density of the Universe at epoch t.

What we want to know is how this acceleration, over time, amounts to particle displacement, and how much extra velocity it imparts to the particles. To that end we need to integrate the acceleration once with respect to time to get velocity, and twice to get the displacement, $d(\mathbf{r},t)$. However the current expression for acceleration, eq. A7, needs to be simplified.

First, remembering that the density distribution in the main peak and perturbation field and growth rate of perturbations are functions of radial position only, we use x instead of $\mathbf{x}$, and r instead of $\mathbf{r}$. Second, our eventual goal is the *rms* value of acceleration, so scalar g will replace vector $\mathbf{g}$. Third, a major simplification is accomplished by decoupling the time dependence of acceleration, i.e. the rate of growth of acceleration, from its spatial variation. Let the initial acceleration field due to secondary perturbations be denoted by $g_0(x)$. Then the dimensionless rate of growth of acceleration is given by,

$$F_g(x,t) = g(x,t)/g_0(x) = g(r,t)/g_0(r). \tag{A8}$$

With these, the proper displacement of a particle can be evaluated as

$$d_p(x,t) = \int_0^t dt_1 \int_0^{t_1} dt_2\ g(x,t_2) = g_0(x) \int_0^t dt_1 \int_0^{t_1} dt_2\ F_g(x,t_2), \tag{A9}$$

and is related to the comoving displacement, $d(x,t) = d_p(x,t)/a(t)$, where $a(t)$ is the scale factor. Next we describe the two functions, $F_g(x,t)$ and $g_0(x)$, separately.

A.4.1. Time evolution of acceleration: $F_g(x,t)$

In the linear growth regime in Einstein-de Sitter Universe model we have, using proper coordinates: $\rho \propto t^{-2}$, $\epsilon \propto t^{2/3}$, and $r \propto t^{2/3}$, so by applying these time scalings to eq. A7 the growth rate of acceleration becomes $F_g(t) \propto t^{-2/3}$, independent of radial position x of the perturbation. This approximation is too crude for our purposes; we suspect that acceleration growth rate of a small patch within the halo will depend on the local conditions at x as well as time. In fact, to simplify the situation RG87 assume that $F_g(x,t)$ depends on the *local* conditions only, so with the help of eq. A7 the acceleration growth rate becomes (RG87 eq.[44][5])

$$F_g(x,\theta) = \frac{g(x,\theta)}{g_0(x)} = \frac{\rho_0[1+\delta(x,\theta)]\epsilon(x,\theta)r(x,\theta)}{\rho_0\epsilon_0 x} = 8\bar{\delta}_0 \frac{f_2(\theta)}{[f_1(\theta) - \frac{\delta_0(x)}{\delta_0(x)}\, f_2(\theta)]^2}, \qquad \text{(A10)}$$

where expressions for $\delta(x,\theta)$, $\epsilon(x,\theta)$ and $r(x,\theta)$ are taken from eqs. A2, A5 and A6. As mentioned earlier, for the period of time prior to turn-around we are free to exchange time t for θ; the relation between the two is fixed by the parametric equations A2 and A3.

A.4.2. Spatial distribution of secondary perturbations: $g_0(x)$

Now we turn our attention to the spatial dependence of acceleration. We are interested in the mean square value of acceleration with respect to the center of the main density peak:

$$[\Delta g_0(\mathbf{x})]^2 = \Big\langle |\mathbf{g}_0(\mathbf{x}_p) - \mathbf{g}_0(\mathbf{x}_c)|^2 \Big\rangle, \qquad \text{(A11)}$$

where $\mathbf{x}_p$ and $\mathbf{x}_c$ are the positions of particle and the center of the halo with respect to some absolute reference frame, and $\mathbf{x} = \mathbf{x}_p - \mathbf{x}_c$ is constant in this calculation. The average is over all the realizations of the Gaussian random field which describes the secondary perturbation field appearing in eq. A7:

$$\epsilon_0(\mathbf{x}) = \frac{1}{(2\pi)^3}\int d^3k\ \epsilon_{\mathbf{k}}\ e^{i\mathbf{k}\cdot\mathbf{x}}, \qquad \langle|\epsilon_{\mathbf{k}}|^2\rangle = P_s(k) \qquad \text{(A12)}$$

A single Fourier mode $\mathbf{k}$ of the $\epsilon_0(\mathbf{x})$ field will produce acceleration of a particle with respect to the center of the halo equal to (see eq. A7)

$$\Delta\mathbf{g}_{0,\mathbf{k}}(\mathbf{x}) = -i4\pi G\rho_0\epsilon_{\mathbf{k}}\frac{\mathbf{k}}{k^2}(e^{i\mathbf{k}\cdot\mathbf{x}_p} - e^{i\mathbf{k}\cdot\mathbf{x}_c}), \qquad \text{(A13)}$$

[5]Note a typo in their paper: $f_1(\theta)$ in the numerator of eq.(44) should be $f_2(\theta)$.

and, by symmetry, directed along the vector $\mathbf{k}$. The square of the magnitude of $\Delta\mathbf{g}_{0,\mathbf{k}}(\mathbf{x})$ is

$$|\Delta g_{0,\mathbf{k}}|^2 = (4\pi G\rho_0/k)^2 P_s(k) 2(1-\cos\mathbf{k}\cdot[\mathbf{x}_p-\mathbf{x}_c]) = (4\pi G\rho_0/k)^2 P_s(k) 2(1-\cos\mathbf{k}\cdot\mathbf{x}), \quad \text{(A14)}$$

and the dependence on the location of the origin has dropped out. Putting all the modes together,

$$[\Delta g_0(x)]^2 = \frac{1}{(2\pi)^3}\int |\Delta g_{0,\mathbf{k}}|^2 d^3k, \quad \text{(A15)}$$

and integrating over the spherically symmetric $\mathbf{k}$ space we can write eq. A11 as

$$\Delta g_0(x) = 4G\rho_0\Big[\int P_s(k)(1-\frac{\sin kx}{kx})dk\Big]^{1/2}. \quad \text{(A16)}$$

By symmetry, this rms acceleration with respect to the center of the halo is a function of particle's initial comoving radius x, and not its 3D position $\mathbf{x}$.

Equation A16 is not yet the final form of $\Delta g_0(x)$. This expression does not discriminate between the different Fourier modes of $\epsilon_0(\mathbf{x})$, allowing all the modes that accelerate the particle at any one instance to contribute to the final acceleration. The reality is somewhat different. Perturbation modes much smaller than the displacement $d(x,t)$ of the particle from its original position, $kd > 1$, are out of phase with the particle, i.e. they can only jiggle the particle about its position contributing to the instantaneous acceleration, but not amounting to any coherent displacement when integrated over time. Since eq. A16 does not take this into account, the short wavelength modes need to be truncated by hand by introducing an exponential cutoff to the power spectrum, $e^{-kd(x,t)}$. Equation A16 now becomes (eq.[38] of RG87),

$$\Delta g_0(d,x) = \frac{2}{3\pi}t_0^{-2}\Big[\int P_s(k)e^{-kd}(1-\frac{\sin kx}{kx})dk\Big]^{1/2}. \quad \text{(A17)}$$

(Note that we have traded the average present day density ρ_0 for the current cosmic time t_0, assuming Einstein-de Sitter cosmology.)

The long wavelength modes of $\epsilon_0(\mathbf{x})$, those with $kx < 1$, do not contribute to the acceleration of the shell with respect to the halo center because they displace the center of the halo and the shell equally. This effect has already been incorporated when deriving eq. A16, the acceleration with respect to the center of the halo. As expected these modes are suppressed, by a factor $(1-\frac{\sin kx}{kx})$ in eq. A16 and eq. A17. These long wavelength modes are important for torquing the halo as a whole, resulting in coherent rotation of the galaxy (see Ryden 1988a).

So the modes that contribute to the net acceleration are the intermediate wavelength modes, $d(x,t) \le k^{-1} \le x$. We emphasize that for different shells, each characterized by an initial comoving radius x and displacement $d(x,t)$, this range of relevant perturbation modes

will be different. Also note that the particle's displacement is assumed to be small compared to its unperturbed distance from the halo's center, $d(x,t) < x$, so that particles always stay close to the shells they originate in.

Having evaluated the spatial (eq. A17) dependence and temporal (eq. A10) evolution of acceleration separately, we can now put them together using eq. A8. Note that because we are interested in accelerations with respect to the halo center, we modify eq. A8 to read: $\Delta g(x,t) = F_g(x,t)\Delta g_0(x)$.

A.4.3. Velocity and displacement of particles due to the $\epsilon(\mathbf{x})$ field

Our goal is to calculate particles' random velocities, which is the time cumulative effect of acceleration. However, $\Delta g_0(d,x)$ in eq. A17 is a function of d for each shell, which is not yet known. To determine $d(x,t)$ we use the fact that acceleration over time amounts to displacement, eq. A9. We introduce a dimensionless growth factor, $F_r(x,t)$ for displacement, related to the acceleration growth factor, $F_g(x,t)$ (eq. A10), and the proper displacement by

$$d_p(x,t) = \Delta g_0(x) \int_0^t dt_1 \int_0^{t_1} dt_2 \; F_g(x,t) = \Delta g_0(x) \; t_0^2 \; F_r(x,t), \tag{A18}$$

The comoving displacement, $d(x,t)$, for an initial comoving label x and time t is given by (eq.[37] of RG87):

$$d(x,t) = d_p(x,t)/a(t) = \Delta g_0(x) \; t_0^2 \; F_r(x,t)/a(t) \tag{A19}$$

We are interested in random velocities at turnaround, which is half of the collapse time, $t = t_c(x)/2$, so we evaluate eq. A19 at that time, when $\theta = \pi$. Using eq. A3 and assuming Einstein-de Sitter evolution of the scale factor, $a(t) = (t/t_0)^{2/3}$, we get

$$d(x, t_c/2) = (\frac{4}{3\pi})^{2/3} \; t_0^2 \; \bar{\delta}_0(x) \; \Delta g_0(d,x) \; F_r(x, t_c/2) \tag{A20}$$

The displacement d appears on both side of this equation, and thus can be solved for in a self-consistent fashion for every shell.

Next, we estimate the magnitude of the extra velocity imparted to a typical dark matter particle at the time of turn-around (eq.[48] of RG87),

$$|\Delta \mathbf{v}_{\rm rms}(x, t_c/2)| = F_v(x, t_c/2) \Delta g_0[d(x, t_c/2), x] t_0, \tag{A21}$$

where velocity growth factor $F_v(x,t)$ is defined similarly to $F_g(x,t)$ and $F_r(x,t)$. Because the secondary perturbations are located randomly within the halo, the direction of $\Delta \mathbf{v}$ at any

given point is random, therefore statistically, i.e. averaging over all the particles in any given shell, the squared magnitude of $\Delta\mathbf{v}_{\rm rms}$ should be divided equally among the three orthogonal directions:

$$(\Delta v_{tan})^2 = \frac{2}{3}|\Delta\mathbf{v}_{\rm rms}(x)|^2, \quad \text{and} \quad (\Delta v_{rad})^2 = \frac{1}{3}|\Delta\mathbf{v}_{\rm rms}(x)|^2. \tag{A22}$$

The magnitude and direction of extra velocity of a typical dark matter particle in a given shell, eq. A21 and eq. A22, are the main quantitative results so far and will be used in the next section as the starting point for the halo collapse. As noted earlier, the dark matter particles' positions are not updated by their respective displacements $d(x, t_c/2)$; we assume that these can be ignored because, being randomly directed they average to zero for any small patch of the halo. RG87 estimate that these displacements are small (see their Fig.9).

A.5. Shell-crossing and equilibrium halo

Before we proceed with the collapse calculation we have to describe the core of the halo, which was already introduced in Section A.1. The density profile of the core can be chosen arbitrarily. The core is dynamically inert, i.e. once set its density distribution is not changed throughout the collapse. The core is required as the starting point, or seed, for the computation of the collapse of overlying shells. From the physical point of view one can imagine that the core consists of the inner most shells that were the very first ones to collapse, and had enough time to come to an equilibrium before the computations described in this paper were started.

The collapse starts from the inner most shell, the one adjacent to the core. When the first shell reaches its r_{max} it collapses and finds its r_{apo} and r_{peri} within the overall halo potential. It is assumed that the potential is changing slowly compared to the dynamical timescales of the shells, so that every shell conserves its adiabatic invariants, the radial and tangential momenta,

$$j_\theta(x) = \Delta v_{tan}\, r_{max} \tag{A23}$$

$$j_r(x) = \int_{r_{peri}}^{r_{apo}} v_{rad}\, dr \tag{A24}$$

throughout the collapse. This is an important assumption in the RG87 formalism, it is crucial to the computation of dynamics of shell crossing.

Up to the moment when a given shell reaches its maximum expansion radius $r_{max}(x)$ at a time $t = t_c(x)/2$ corresponding to $\theta = \pi$, the shell is assumed to be thin, its radial extent

determined by the initial shell separation. At r_{max}, the average dark matter particle in the shell is given its additional random velocity, eq. A21 and eq. A22. Because the distribution of the secondary perturbations in the halo is random the phase of $\Delta\mathbf{v}_{\rm rms}$ need not be the same for all the particles in a given shell. In other words, at r_{max} one particle can get an outward kick (positive Δv_{rad}), while another, an inward kick (negative Δv_{rad}) of the same rms amplitude. This makes the shell 'puff up' resulting in a radial distribution of dark matter particles of a given shell between apocenter and pericenter, r_{apo} and r_{peri}. It is important to remember that the halos are assumed to be made of collisionless dark matter particles with negligible interaction cross-section, so that the particles can go through each other without generating shocks or dissipating energy and momentum.

An alternative way of looking at the effect of $\Delta\mathbf{v}_{\rm rms}$ is that all particles of a given shell at r_{max} got kicked 'in phase'. Then the time average, taken over some reasonably long (but shorter than the timescale of evolution of the shell) Δt, will show a distribution of particles in radii, again bounded by r_{apo} and r_{peri}.

In either case the apocenter and pericenter can be calculated from the particle's energy integral and Δv_{tan} and Δv_{rad}. The energy integral,

$$E = \psi(r_{max}) + \frac{1}{2}|\Delta\mathbf{v}_{\rm rms}|^2, \tag{A25}$$

can be considered constant while a shell is still expanding.

The radial velocity of a particle is

$$v_{rad} = [2(E - \psi(r)) - (j_\theta/r)^2]^{1/2}, \tag{A26}$$

[6]

Apocenter and pericenter are the radii where v_{rad} becomes 0; at radii outside of this range the radial velocity is imaginary. The radial distribution of mass within a shell between apocenter and pericenter is not uniform. The density in the radial range dr around r is proportional to the amount of time the particle spends there, (eq.[53] of RG87),

$$P(r)\ dr = \frac{v_{rad}^{-1}\ dr}{\int_{r_{peri}}^{r_{apo}} v_{rad}^{-1}\ dr}. \tag{A27}$$

After the first shell has collapsed the halo has a new radial density distribution, and so the halo's potential has to be recalculated before the second shell starts to collapse.

[6]Note that RG87 define their energy integral and potential as the negatives of the conventional definitions of these quantities. We use the conventional definitions, i.e. potential is negative quantity inside the halo, and energy integral of a bound particle is negative.

The potential contribution from the first shell is evaluated using eq. A27. As the second shell collapses its pericenter will be closer to the center of the halo than the apocenter of the first shell, so the shells will overlap. This is the beginning of shell-crossing. As every additional shell falls in and finds its apo- and pericenter (that satisfy its j_θ, j_r conservation) the potential has to be recalculated, and hence the apo- and pericenters of all the interior shells that overlap the most recently fallen one.

As time goes by the gravitational potential interior to any given shell grows slightly deeper because of the collapse of the inner shells, and on average every shell sinks further into the potential well. This goes on until the present time is reached.

REFERENCES

Avila-Reese, V., Colin, P., Valenzuela, O., D'Onghia, E. & Firmani, C. 2001, ApJ, 559, 516

Avila-Reese, V., Firmani, C. & Hernndez, X. 1998, ApJ, 505, 37

Bardeen, J.M., Bond, J.R., Kaiser, N. & Szalay, A.S. 1986, ApJ, 304, 15

de Blok, W. J. G. & Bosma, A. 2002, A&A, 385, 816

de Blok, W. J. G., McGaugh, S. S., Bosma, A. & Rubin, V. C. 2001, ApJ, 552, 123

Bode, P., Ostriker, J. P. & Turok, N. 2001, ApJ, 556, 93

Bothun, G., Impey, C. & McGaugh, S. 1997, PASP, 109, 745

Bullock, J.S., Dekel, A., Kolatt, T. S., Kravtsov, A.V., Klypin, A. A., Porciani, C. & Primack, J. R. 2001, ApJ, 555, 240

Carlberg, R. G., Yee, H. K. C., Ellingson, E., Morris, S. L., Abraham, R., Gravel, P., Pritchet, C. J., Smecker-Hane, T., Hartwick, F. D.A., Hesser, J. E., Hutchings, J. B. & Oke, J. B. 1997, ApJ, 485, 113

Croft, R. A. C.& Gaztanaga, E. 1998, ApJ, 495, 554

Dalcanton, J. J. & Bernstein, R, A. 2000, AJ, 120, 203

Del Popolo, A., Gambera, M., Recami, E. & Spedicato, E. 2002, A&A, 353, 427

Dubinski, J. & Carlberg, R. G, 1991, ApJ, 369, 13

Eke, V. R., Cole, S. & Frenk, C. S. MNRAS, 282, 263

Ghigna, S., Moore, B., Governato, F., Lake, G., Quinn, T., & Stadel, J. 1998, MNRAS, 300, 146

Gott, J. R. 1975, ApJ, 201, 296

Gunn, J. E. 1977, ApJ, 218, 592

Gunn, J. E. & Gott, J. R. 1972, ApJ, 176, 1

Fillmore, J. A., Goldreich, P. 1984, 281, 1

Frenk, C. S., Whiter S. D. M., Davis, M. & Efstathiou, G. 1988, ApJ, 327, 507

Fukushige T. & Makino, J, 2001, ApJ, 557, 533

Hernandez, X., Avila-Reese. V. & Firmani, C. 2001, MNRAS, 327, 329

Hiotelis, N. 2002, A&A, 383, 84

Hoffman, Y. & Shaham, J. 1985, ApJ, 297, 16

Hozumi, S., Burkert, A., Fujiwara, T. 2000, MNRAS, 311, 377

Huss, A., Jain, B. Steinmetz, M. 1999, ApJ, 517, 64

Jaffe, A. H. *et al.* . 2001, PhysRevL, 86, 3475

Jesseit, R., Naab, T. & Burkert, A. 2002, ApJL, 571, L89

Jing, Y. P. & Suto, Y. 2000, ApJ, 529, L69

Klypin, A., Kravtsov, A. V., Bullock, James S. & Primack, J. R. 2001, ApJ, 554, 903

Knebe, A., Devriendt, J. E. G., Mahmood, A. & Silk, J. 2002, MNRAS, 329, 813

Kull, A. 1999, ApJ, 516, L5

Lokas, E. L. 2000, MNRAS, 311, 432

Lokas, E. L. & Hoffman, Y. 2000, ApJ, 542, L139

Marchesini, D., D'Onghia, E., Chincarini, G., Firmani, C., Conconi, P.,Molinari, E., & Zacchei, A. 2002, ApJ, 575, 801

Mellier, Y. *et al.* . 2001, in ESO Proceedings "Deep Fields", Garching Oct 9-12, 2000

Moore, B., Governato, F., Quinn, T., Stadel, J. Lake, G. 1998, ApJ, 499, L5

Navarro, J. F., Frenk, C. S. & White, S. D. M. 1996, ApJ, 462, 563

Navarro, J. F., Frenk, C. S. & White, S. D. M. 1997, ApJ, 490, 493

Navarro, J. F. & Steinmetz, M. 2000, ApJ, 538, 477

Nusser, A. 2001, MNRAS, 325, 1397

Peebles, P. J. E. 1984, ApJ, 277, 470

Peebles, P. J. E. 1980, *The Large Scale Structure of the Universe*, Princeton University Press

Peebles, P. J. E. 1969, ApJ, 155, 393

Power, C., Navarro, J. F., Jenkins, A., Frenk, C. S., White, S. D. M., Springel, V., Stadel, J., & Quinn, T. 2003, MNRAS, 338, 14

Quinn, P. J., Salmon, J. K. & Zurek, W. H. 1986, Nature, 322, 329

Ryden, B. S. 1988a, ApJ, 329, 589

Ryden, B. S. 1988b, ApJ, 333, 78

Ryden, B. S., Gunn, J. E. 1987, ApJ, 318, 15 (RG87)

Salucci, P. 2001, MNRAS, 320, L1

Salucci, P. & Burkert, A. 2000, ApJ, 537, 19

Spergel, D.N. *et al.* . 2003, preprint, http://xxx.lanl.gov/abs/astro-ph/0302209

Swaters, R. A., Madore, B. F., van den Bosch, F. C., & Balcells, M. 2002, ApJ, in press

Swaters, R. A., Madore, B. F. & Trewhella, M. 2000, ApJ, 531,1107

Syer, D. & White S. D. M. 1998, MNRAS, 293, 337

Subramanian, K., Cen, R., Ostriker, J. P. 1999, ApJ, 538, 528

van den Bosch, F. C., Abel, T., Croft, R. A. C., Hernquist, L. & White S. D. M. 2002, ApJ, 576, 21

van den Bosch, F. C. & Swaters, R. A. 2001, MNRAS, 325, 1017

Weldrake, D., de Blok, E., & Walter, F. 2002, MNRAS, in press

Zaroubi, S. & Hoffman, Y. 1993, ApJ, 416, 410

Zentner, A. R. & Bullock, J. S. 2002, PhysRevD, 66, 3003

This preprint was prepared with the AAS LaTeX macros v5.0.

Table 1. Analytical Secondary Infall Models at a Glance

Paper	Initial density profile shape	Cutoff radius	Nonradial Motions	Self-sim.?	Conserved quantities	Final density profile
GG72	δ-fcn	none	none	yes	none	power law
G77	δ-fcn	none	none	yes	$J_r = r\,m(r)$	power law
FG84	power law	none	none	yes	J_r	power law
HS85	corr. fcn.	none	none	yes	J_r	power law
RG87	peaks	none	sec. perturb.	no	J_r, J_θ	concave
ZH93	power law	none	none	yes	J_r	power law
AFH98	MAH	none	thermal motions	no	J_r, J_θ	concave
L00	corr. fcn.	$\frac{1}{2}d_{\rm peak-peak}$	none	no	J_r	concave
N00	power law	none	2 analyt. schemes	yes	J_r, J_θ	concave

References. — Gunn & Gott (1972); Gunn (1977); Fillmore & Goldreich (1984); Hoffman & Shaham (1985); Ryden & Gunn (1987); Zaroubi & Hoffman (1993); Avila-Reese, Firmani & Hernandez (1998); Lokas (2000); Nusser (2001).

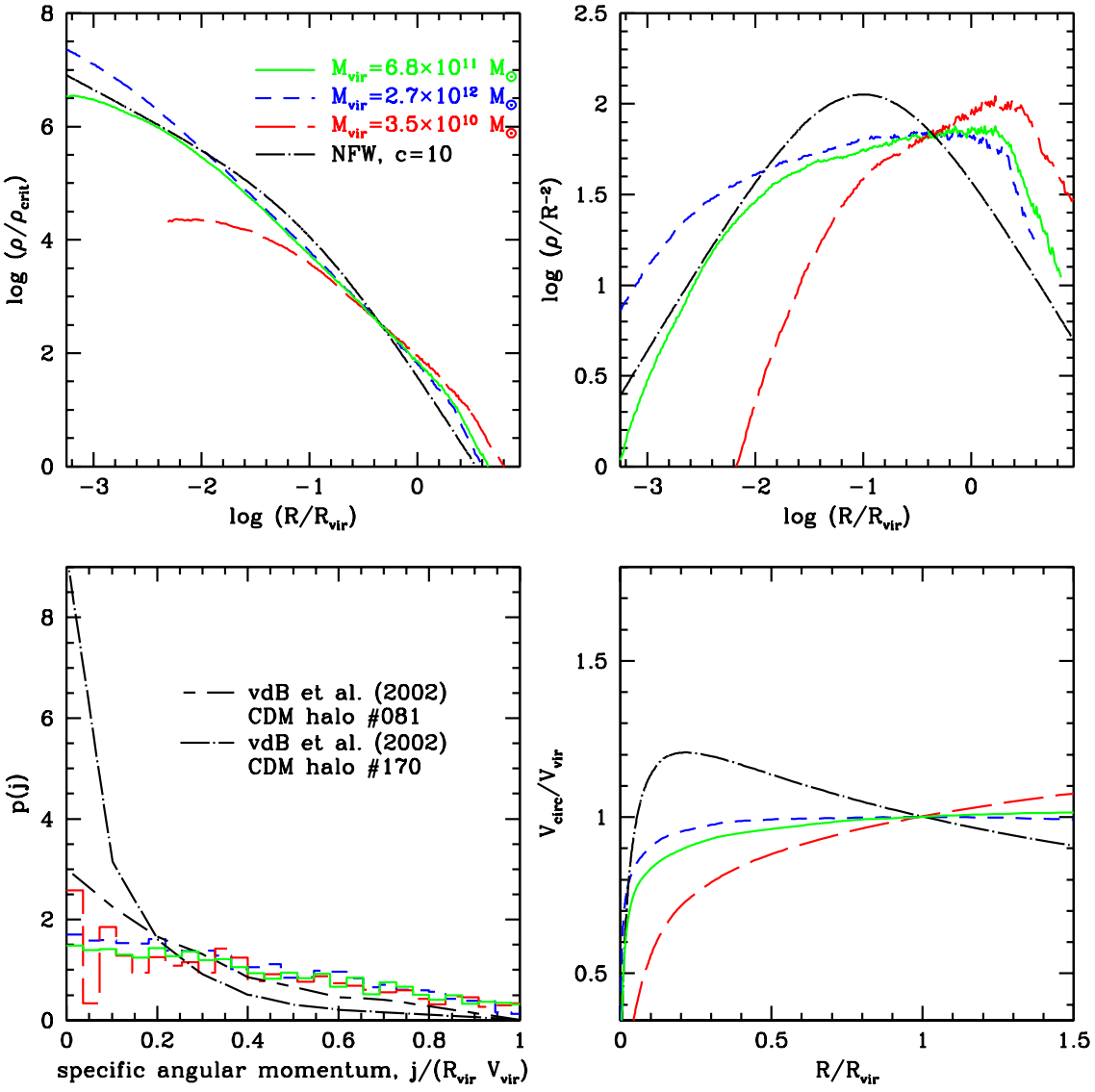

Fig. 1.— Dark matter halos generated using "standard" initial conditions, as described in Section 4.3. Halos of three different galactic-type masses are shown; the intermediate mass halo (solid line) is the 'reference' halo. *Upper left:* log-log density profiles. The lowest mass halo is not resolved at $\lesssim 1\%$ of R_{vir}. NFW $c = 10$ halo is shown for comparison (dot-dash line). *Upper right:* density profiles with the slope of $\alpha = 2$ divided out, so $\alpha = 2$ slopes are flat in this plot. *Lower right:* circular rotation curves. *Lower left:* the distribution of specific angular momenta (SAM) in our halos, as histograms. For comparison, we include two extreme SAM distributions taken from N-body simulations of van den Bosch *et al.* (2002).

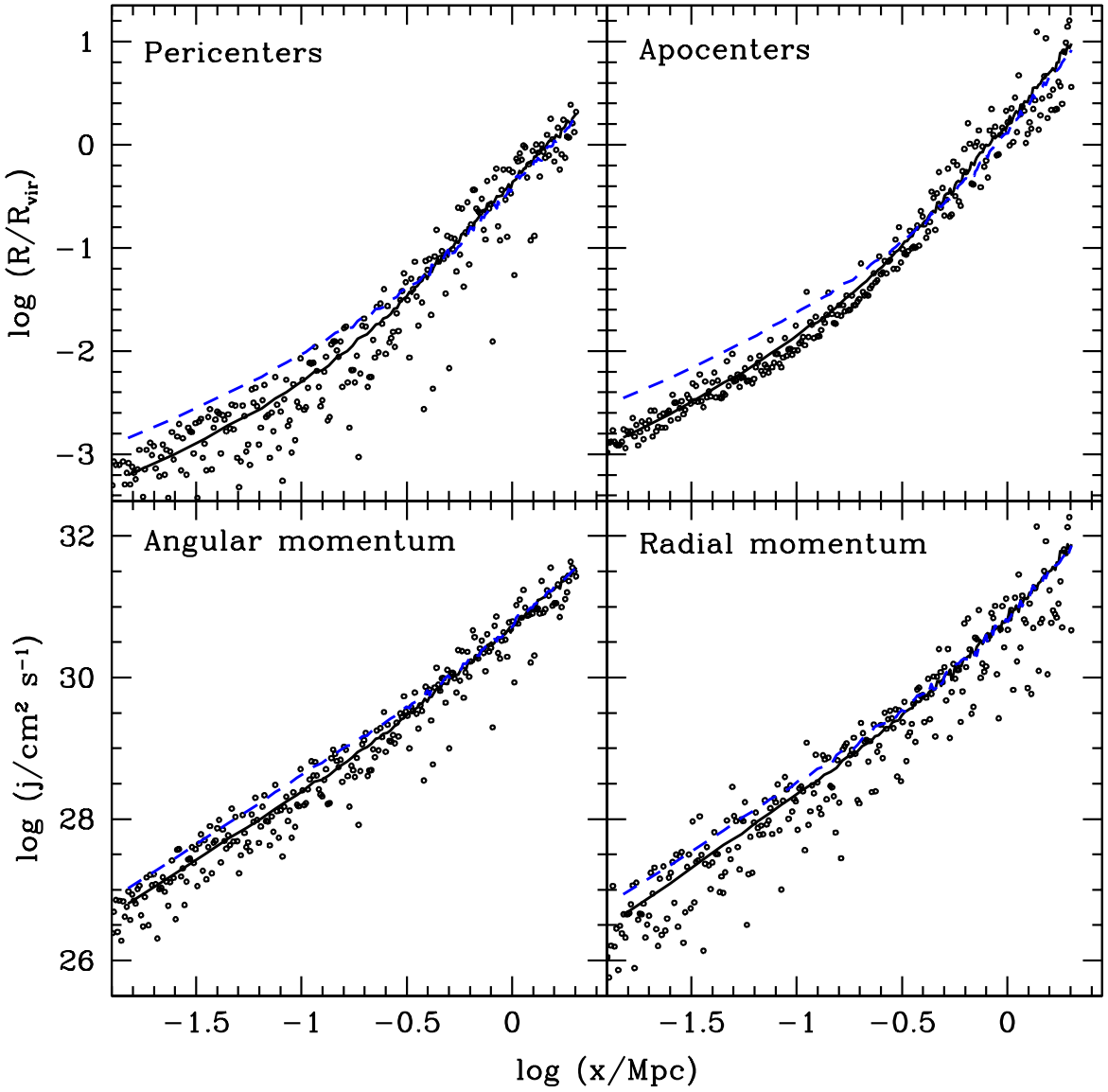

Fig. 2.— Top panels shows apo- and pericenters, while bottom panels show angular and radial momenta of individual shells (solids dots), and averaged over shells from many halos at the same initial comoving position, x (lines). Solid lines and points represent the reference halo, Section 4.3. The dashed lines represent halos generated using a smoothed power spectrum with $r_f = 0.1$ Mpc (Section 4.6). Notice the scatter in properties from shell to shell. Also note that shells in halos with less fluctuation power on small scales (dashed lines) have more angular and radial momentum and do not penetrate deep into halo's interior (see Section 5.5.)

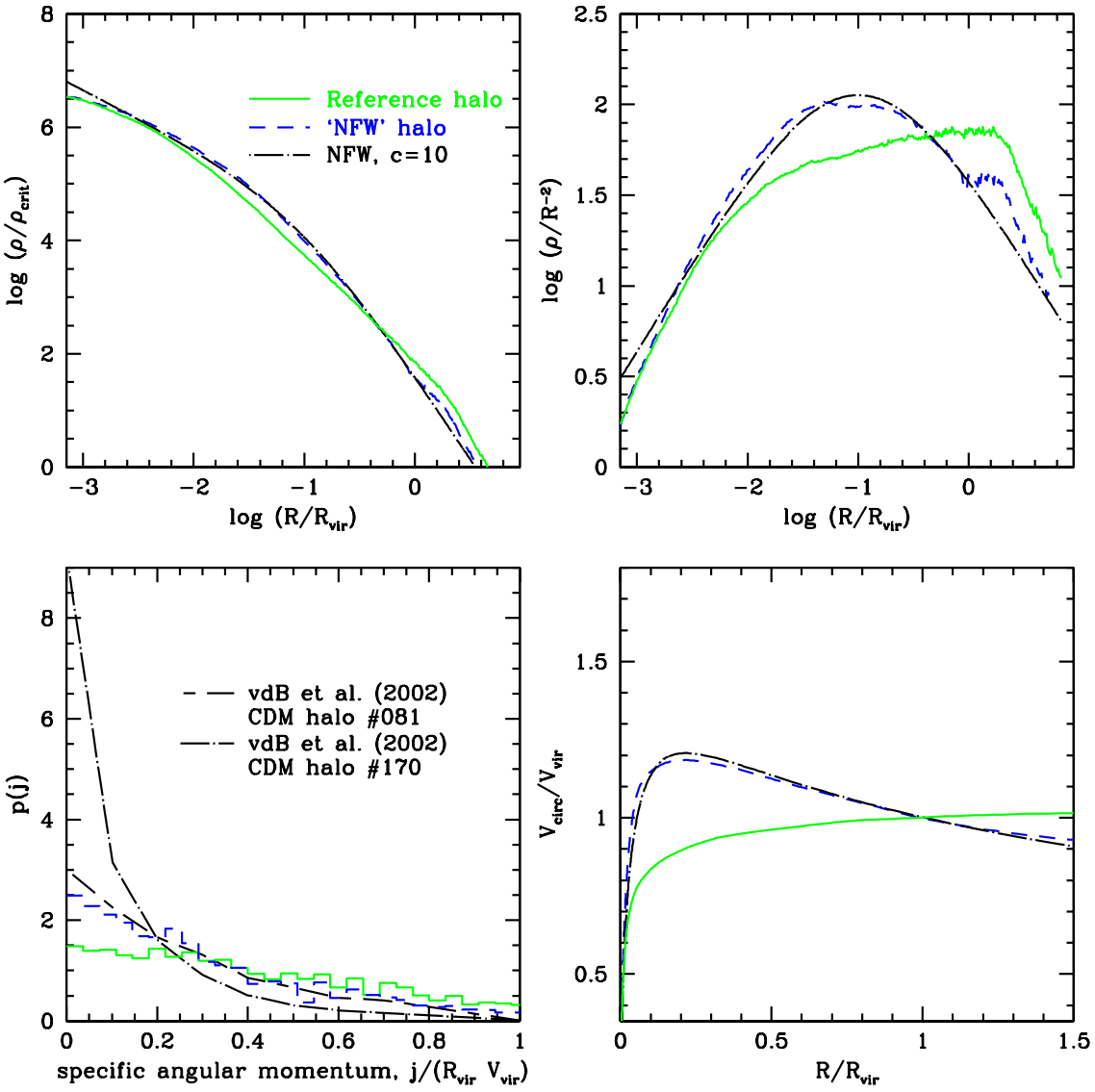

Fig. 3.— Same as Fig. 1, but here we attempt to reproduce a $c = 10$ NFW halo. Starting with our reference halo (Section 4.3) we reduced the amplitudes of the random velocities of particles that ended up roughly between 0.1 and 1 R_{vir}. The SAM distribution of this halo (dashed histogram in the lower left panel) is similar to that of N-body halo #081 (van den Bosch *et al.* 2002). See Section 4.4 for details.

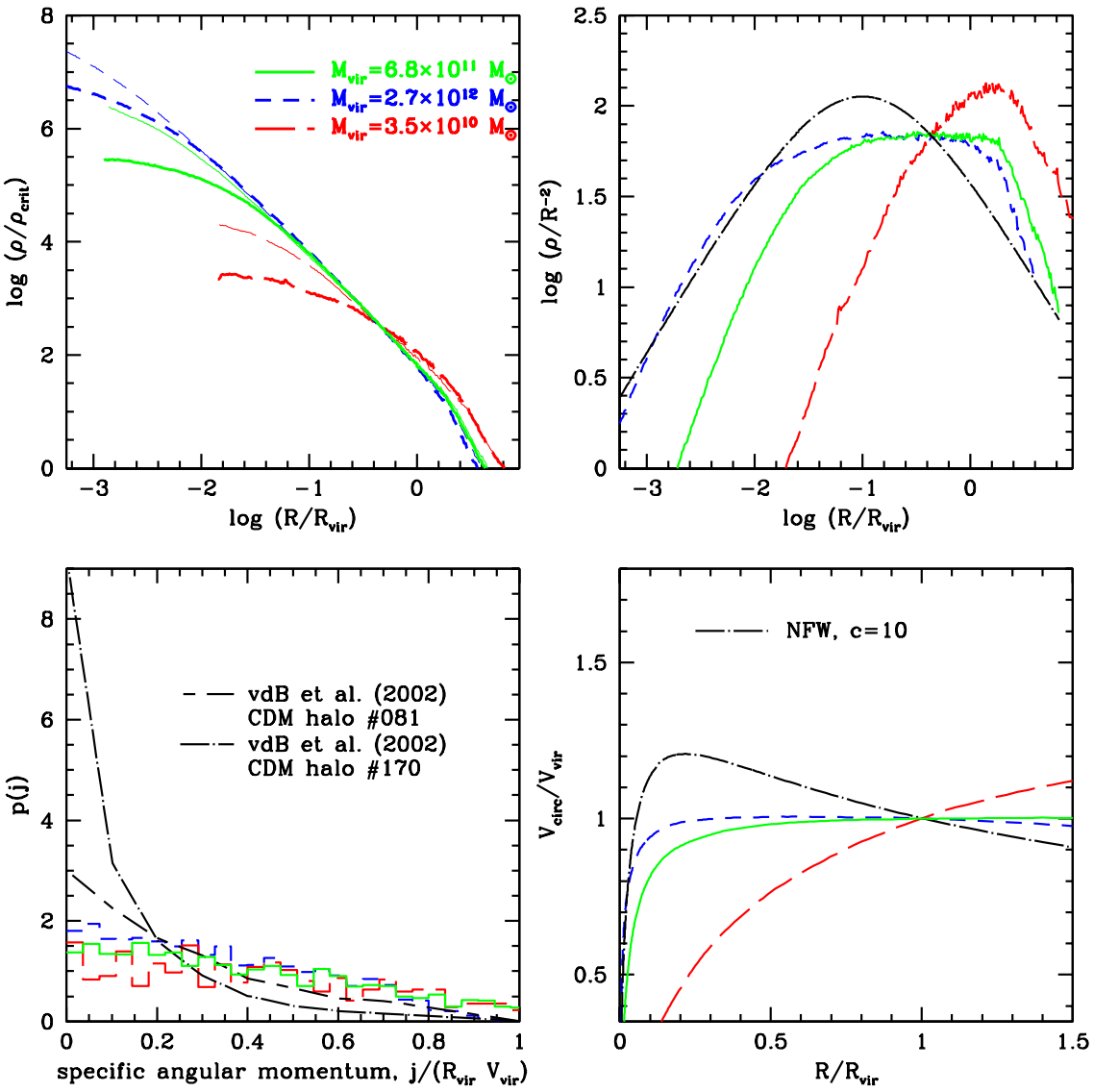

Fig. 4.— Same as Fig. 1, but for filtered initial power spectrum: The halos here are the same as in that figure, except that $r_f = 0.1$ Mpc has been applied to $P(k)$. The masses of the three halos are similar to those of the corresponding halos in Fig. 1. For comparison, we show the three halos from Fig. 1 as thin lines in the upper left panel; the NFW profile has been omitted in this panel. See Section 4.6 for details.

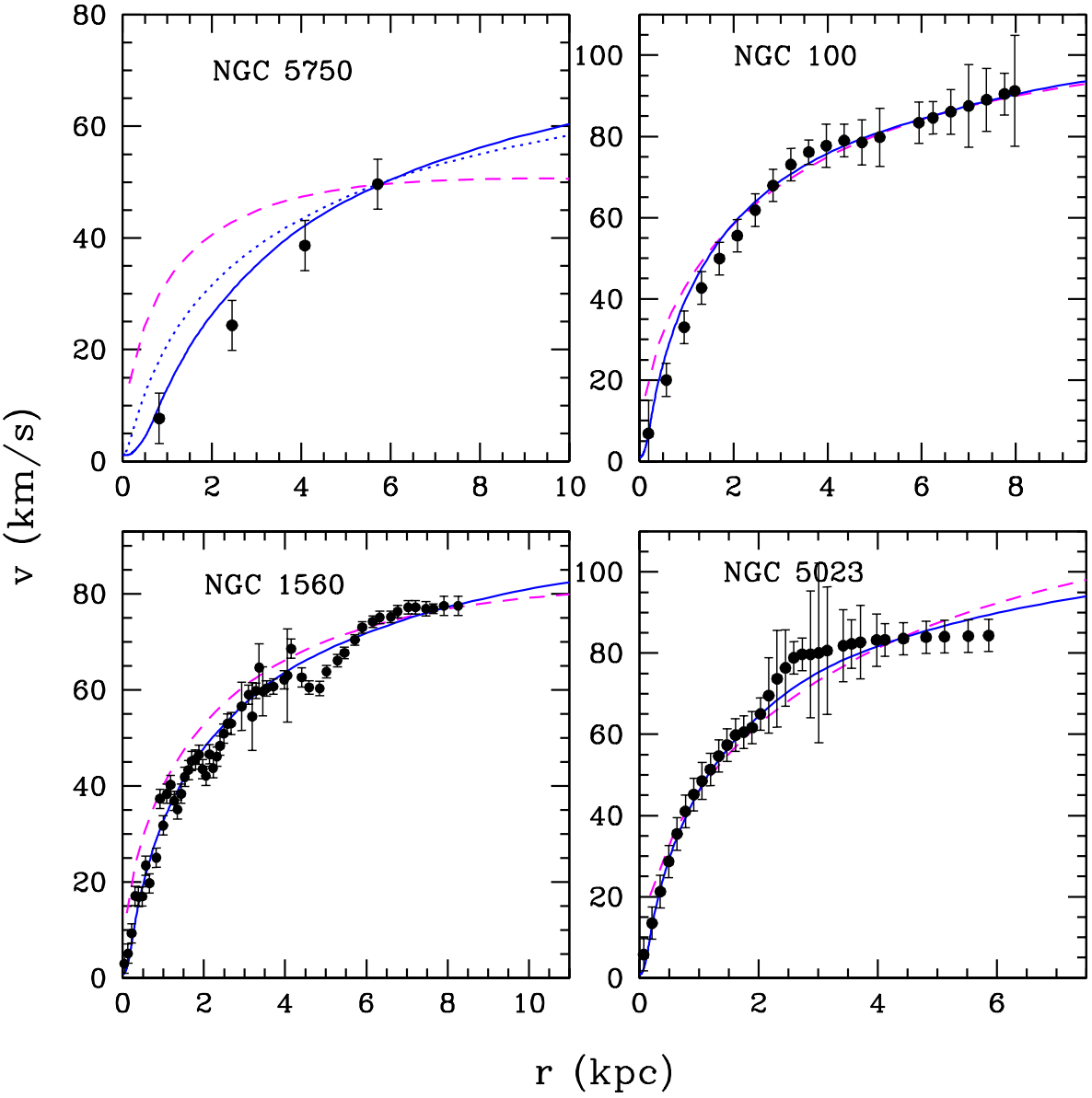

Fig. 5.— The points with error-bars are the high-resolution rotation curves of LSB galaxies taken from de Blok & Bosma (2002). The dashed lines are NFW fits obtained by adjusting 1 parameter: c varies between 13.5 and 17 for these galaxies. The solid lines are our halos with tangentailly oriented velocity ellipsoids: $\zeta_0 = 20°$ for NGC 5750 and NGC 100, and $\zeta_0 = 50°$ for NGC 1560 and NGC 5023. The dotted curve in the upper left represents our halo with a spherical velocity ellipsoid, i.e. $\zeta_0 = 90°$. See Section 4.7 for details.

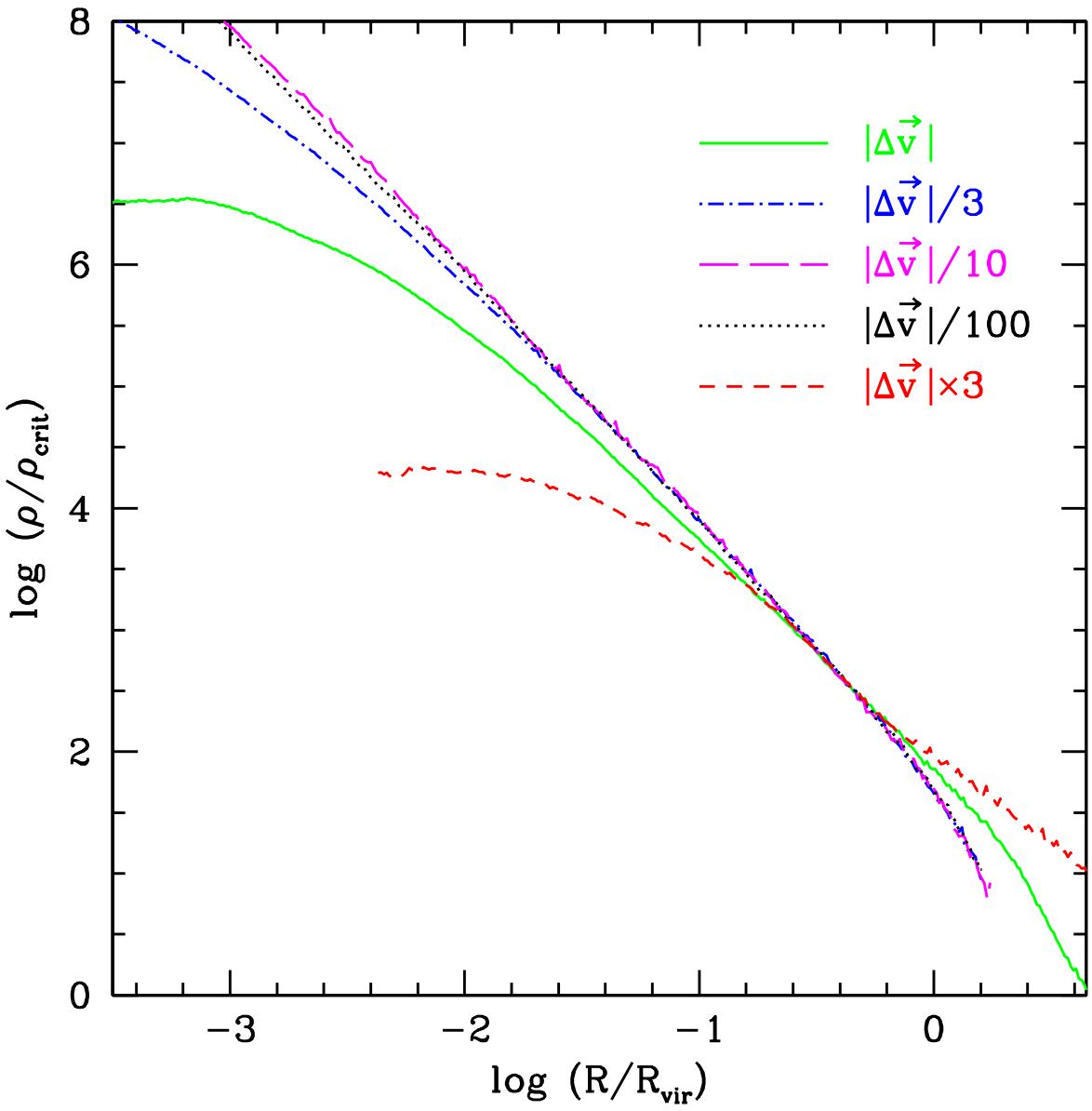

Fig. 6.— Density profiles of halos whose random particle velocities have been reduced by factors of 3 (dot-dash), 10 (long dash) and 100 (dotted), and increased by a factor of 3 (short dash), compared to the reference halo (solid line). Reducing random velocities means that the angular momentum of dark matter particles is reduced, which results in steeper central density slopes. The limiting slope, $\alpha = 2$ is discussed in Section 5.1, and the progressive shallowing of the slopes in Section 5.3.

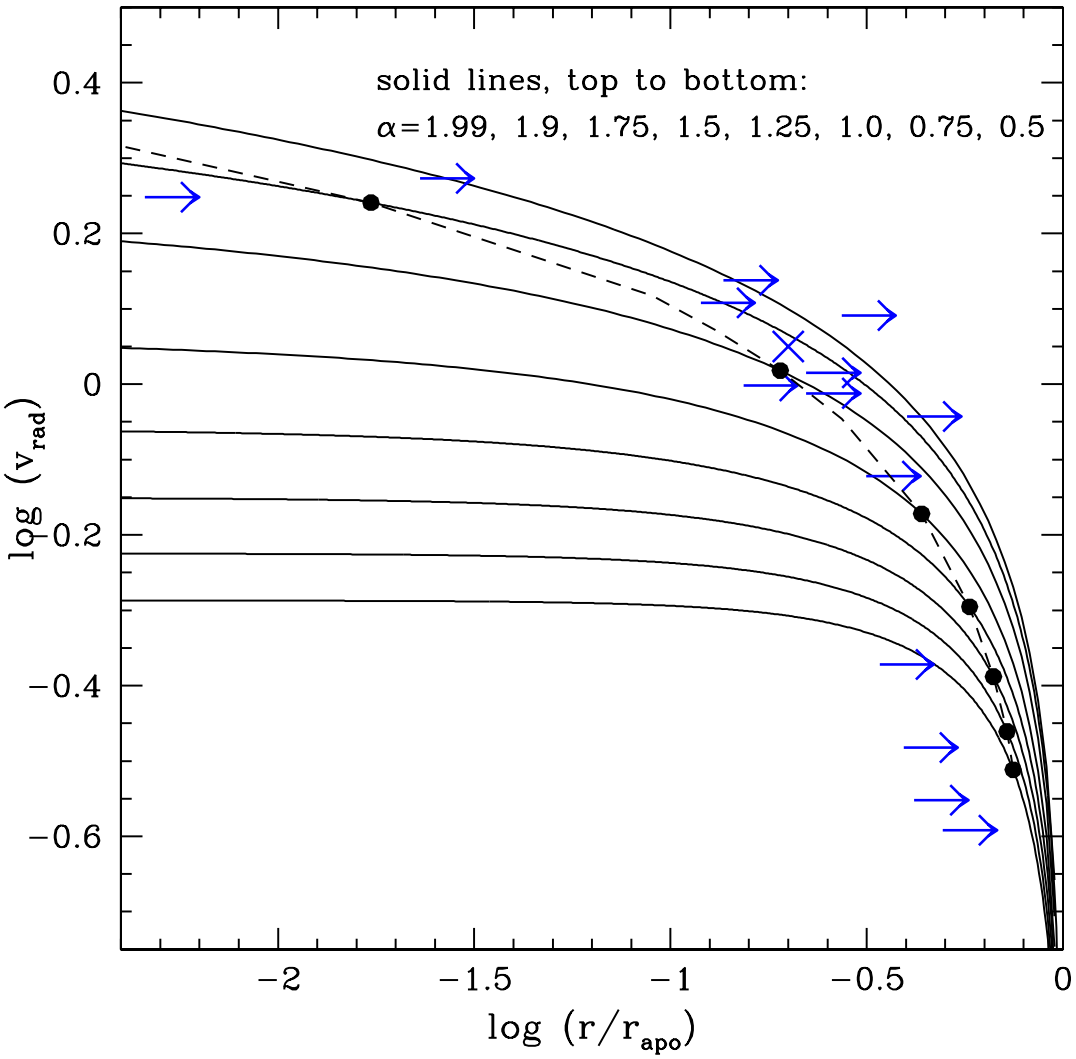

Fig. 7.— Radial velocity vs. radial position of particles (or shells) in dark matter halos. The solid lines are solutions of Eq. 5 for a range of halo inner slope values α. The solid dots connected by a dashed line are the predictions of an analytic model: the points satisfy both Eq. 5 and the condition $v_{rad} \propto r^{\alpha-2}$; see Section 5.1 for details. Horizontal arrows represent data taken from our dark matter halos; the cross symbol at (-0.70, 0.05) represents high resolution N-body halo of Ghigna *et al.* (1998); see Section 5.2 for more details.

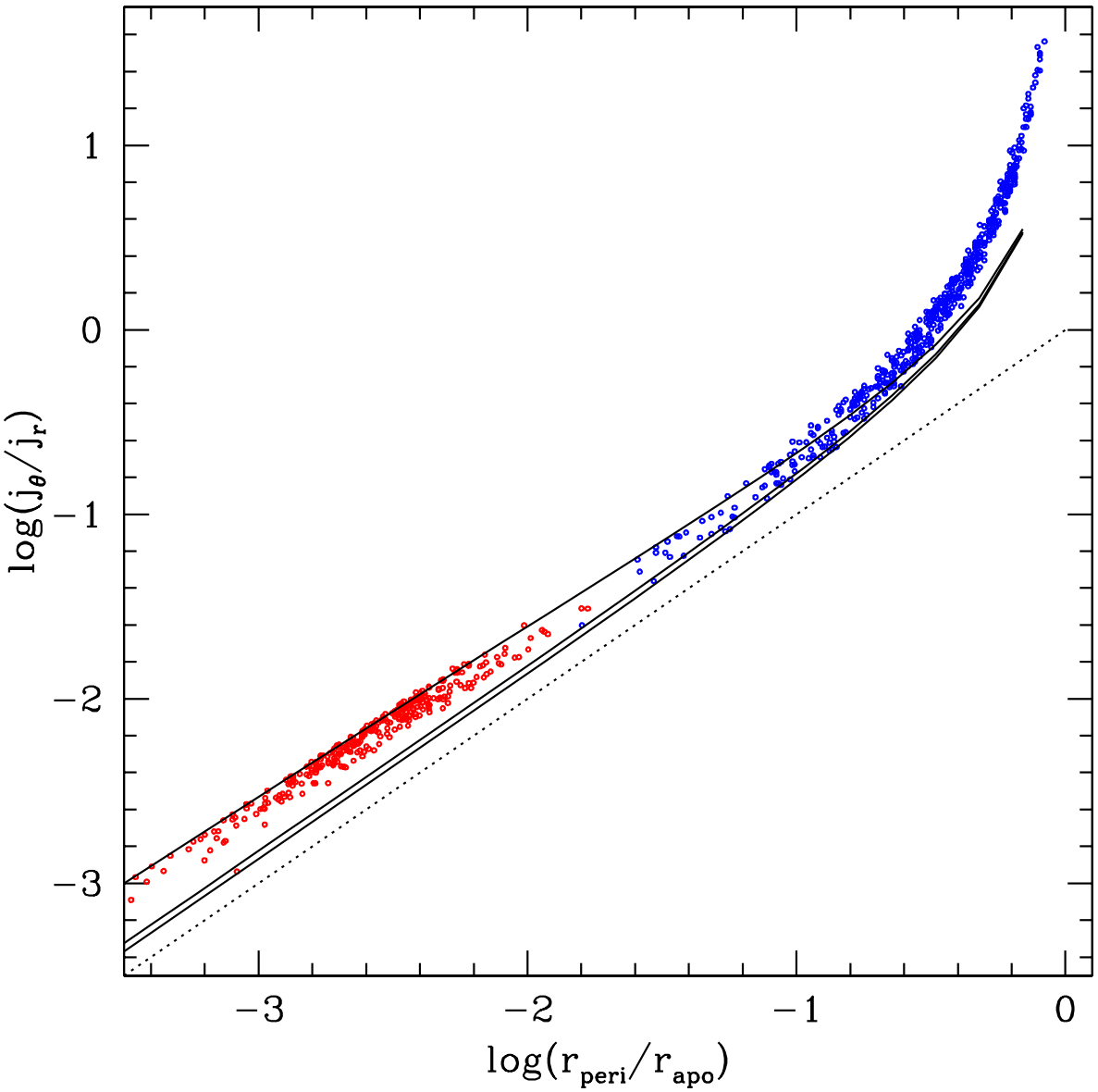

Fig. 8.— A relation between r_{peri}/r_{apo} and j_θ/j_r for shells in our halos. In spite of the dispersion in individual shell properties (shown in Fig. 2) all shells in all halos obey this well defined relation, which can be understood in terms of the model presented in Section 5. The three solid lines are predictions of this model for non-circular orbits in halos with $\alpha = 1.99$, 1, and 0.5 (top to bottom). The dotted line is the relation $r_{peri}/r_{apo} = j_\theta/j_r$. Circular orbits will lie at $r_{peri}/r_{apo} = 1$ and $j_\theta/j_r \to \infty$ There are two sets of points: the upper right set belongs to the reference halo (Section 4.3), while the lower left set belongs to the halo with almost no random motions, shown as the dotted line in Fig. 6. See Section 5.4 for details.

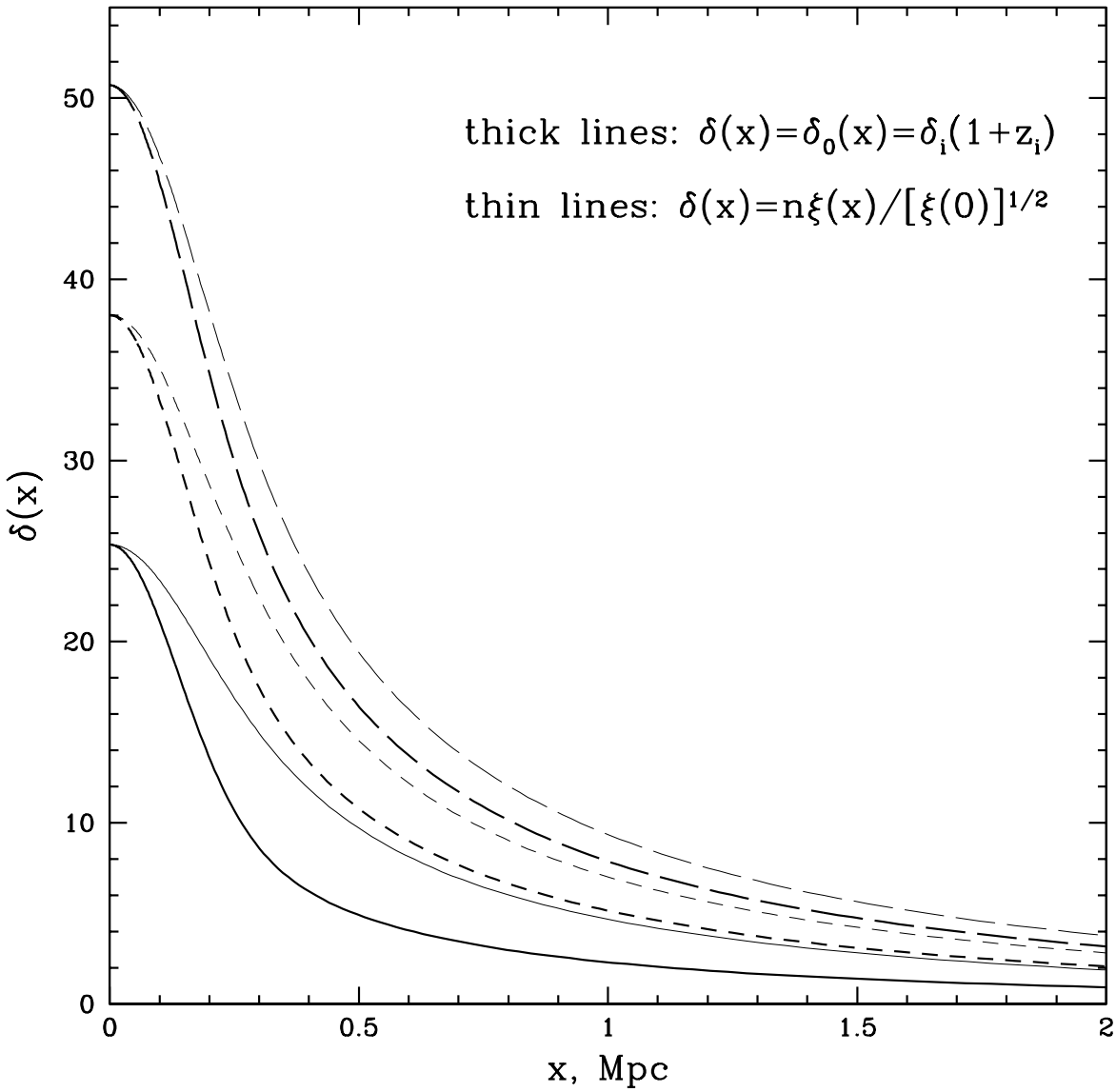

Fig. 9.— Initial density profiles of dark matter halos (see Section A.1). Thin lines (the higher of each of the three sets of lines) are proportional to the two-point correlation function, and represent density run averaged around local density maxima or minima in the initial Gaussian random field. Solid, short dashed, and long dashed lines represent 2, 3, and 4 σ peaks. Thick lines are density profiles around maxima only, and are used as the initial profiles of proto-halos in our computations.